Cell-type specialization in the brain is encoded by specific long-range chromatin topologies

Warren Winick-Ng[1,#], Alexander Kukalev[1,#], Izabela Harabula[1,2,#], Luna Zea Redondo[1,2,&], Dominik Szabo[1,2,&], Mandy Meijer[3], Leonid Serebreni[1,a], Yingnan Zhang[4], Simona Bianco[5], Andrea M. Chiariello[5], Ibai Irastorza-Azcarate[1], Luca Fiorillo[5], Francesco Musella[5], Christoph J. Thieme[1], Ehsan Irani[1,6], Elena Torlai Triglia[1,b], Aleksandra A. Kolodziejczyk[7,8,c], Andreas Abentung[9,d], Galina Apostolova[9], Eleanor J. Paul[10,e], Vedran Franke[11], Rieke Kempfer[1,2], Altuna Akalin[11], Sarah A. Teichmann[7,8], Georg Dechant[9], Mark A. Ungless[10], Mario Nicodemi[5,6], Lonnie Welch[4], Gonçalo Castelo-Branco[3,12], Ana Pombo[1,2,6,*]

[1]Epigenetic Regulation and Chromatin Architecture Group, Berlin Institute for Medical Systems Biology, Max-Delbrück Centre for Molecular Medicine, 10115 Berlin, Germany
[2]Humboldt-Universität zu Berlin, 10117 Berlin, Germany
[3]Laboratory of Molecular Neurobiology, Department of Medical Biochemistry and Biophysics, Karolinska Institutet, 17177 Stockholm, Sweden
[4]School of Electrical Engineering and Computer Science, Ohio University, 45701 Athens, OH, USA
[5]Dipartimentio di Fisica, Università di Napoli Federico II, and INFN Napoli, Complesso Universitario di Monte Sant'Angelo, 80126 Naples, Italy
[6]Berlin Institute of Health, 10178 Berlin, Germany
[7]Cavendish Laboratory, University of Cambridge, JJ Thomson Ave, Cambridge CB3 0EH, UK
[8]Wellcome Sanger Institute, Wellcome Genome Campus, Hinxton, Cambridge CB10 1SA, UK
[9]Institute for Neuroscience, Medical University of Innsbruck, 6020 Innsbruck, Austria
[10]Institute of Clinical Sciences, Imperial College London, London SW7 2AZ, UK
[11]Bioinformatics and Omics Data Science Platform, Berlin Institute for Medical Systems Biology, Max-Delbrück Centre for Molecular Medicine, 10115 Berlin, Germany
[12]Ming Wai Lau Centre for Reparative Medicine, Stockholm node, Karolinska Institutet, 17177 Stockholm, Sweden

[a]current address: Research Institute of Molecular Pathology (IMP), 1030 Vienna Biocenter (VBC), Vienna, Austria
[b]current address: Broad Institute of MIT and Harvard, 02142 Cambridge, MA, USA
[c]current address: Immunology Department, Weizmann Institute of Science, 7610001 Rehovot, Israel
[d]current address: Department of Clinical and Molecular Medicine, Norwegian University of Science and Technology, 7491 Trondheim, Norway
[e]current address: Center for Developmental Neurobiology, Institute of Psychiatry, Psychology and Neuroscience, King's College London, London WC2R 2LS, UK; MRC Center for Neurodevelopmental Disorders, King's College London SE1 1UL, UK

[#]These authors contributed equally to this work
[&]These authors contributed equally to this work

*Corresponding author: ana.pombo@mdc-berlin.de

Abstract

Neurons and oligodendrocytes are terminally differentiated cells that sustain cascades of gene activation and repression to execute highly specialized functions, while retaining homeostatic control. To study long-range chromatin folding without disturbing the native tissue environment, we developed Genome Architecture Mapping in combination with immunoselection (immunoGAM), and applied it to three cell types from the adult murine brain: dopaminergic neurons (DNs) from the midbrain, pyramidal glutamatergic neurons (PGNs) from the hippocampus, and oligodendroglia (OLGs) from the cortex. We find cell-type specific 3D chromatin structures that relate with patterns of gene expression at multiple genomic scales, including extensive reorganization of topological domains (TADs) and chromatin compartments. We discover the loss of TAD insulation, or 'TAD melting', at long genes (>400 kb) when they are highly transcribed. We find many neuron-specific contacts which contain accessible chromatin regions enriched for putative binding sites for multiple neuronal transcription factors, and which connect cell-type specific genes that are associated with neurodegenerative disorders such as Parkinson's disease, or specialized functions such as synaptic plasticity and memory. Lastly, sensory receptor genes exhibit increased membership in heterochromatic compartments that establish strong contacts in brain cells. However, their silencing is compromised in a subpopulation of PGNs with molecular signatures of long-term potentiation. Overall, our work shows that the 3D organization of the genome is highly cell-type specific, and essential to better understand mechanisms of gene regulation in highly specialized tissues such as the brain.

27 ***Introduction***

28 The study of three-dimensional (3D) chromatin organization has revealed its
29 intrinsic association with gene regulation and cell function[1]. Genome-wide
30 sequencing approaches such as Hi-C[2], GAM[3] and SPRITE[4] have shown that the
31 genome is organized hierarchically, from specific promoter-enhancer contacts, to
32 topologically associating domains (TADs), to broader compartments of open and
33 closed chromatin (compartments A and B, respectively), up to whole chromosome
34 territories[2-5]. Dynamic changes of chromatin organization during neuronal
35 development have been reported using *in-vitro* differentiated neurons, or
36 glutamatergic neurons obtained after cortical tissue dissociation and FACS isolation
37 from pools of animals, or from mixed cell populations from whole hippocampi[6-8].
38 However, it has been difficult to assess chromatin structure of specific cell types from
39 the brain, especially without disrupting tissue organization, and in single animals.
40 Understanding 3D chromatin structure of specialized cell populations is of
41 exceptional importance in the brain, where connecting disease-associated genetic
42 variants in non-coding genomic regions with their target genes remains challenging,
43 and where cell state and localization within the tissue can influence both
44 transcriptional and physiological outcomes.

45

46 ***ImmunoGAM maps 3D genome architecture in specific mouse brain***

47 Here we developed immunoGAM, an extension of the Genome Architecture
48 Mapping (GAM) technology[3] to perform genome-wide mapping of chromatin topology
49 in specific cell populations. GAM is a ligation-free technology that maps 3D genome
50 topology by extracting and sequencing the genomic DNA content from nuclear
51 cryosections, followed by detection of 3D chromatin interactions from the increased
52 probability of co-segregation of genomic loci across a collection of nuclear slices,

53 each from a single nucleus. GAM was previously applied to mouse embryonic stem
54 cells (mESCs) and shown to capture TADs, A/B compartments and pair-wise
55 contacts across long genomic distances[3]. Recently, we developed a streamlined
56 version of GAM, multiplexGAM, which combines three nuclear slices in each GAM
57 sample[9]. With immunoGAM, we now considerably extend the scope of GAM to
58 directly work in intact tissue without prior dissociation, and with small cell numbers
59 (~1000 cells)[3,10].
60
61 To explore how genome folding is related with cell specialization, we applied
62 immunoGAM in three specific brain cell types with diverse functions (**Fig. 1a**). We
63 selected oligodendroglia (oligodendrocytes and their precursors; OLGs) from the
64 somatosensory cortex, as they are involved in myelination of neurons and influence
65 neuronal circuit formation[11]. Pyramidal glutamatergic neurons (PGNs) were selected
66 from the *cornu ammonis 1* (CA1) region of the dorsal hippocampus. PGNs have
67 specialized roles in temporal and spatial memory formation and consolidation, and
68 are activated intrinsically and frequently[12,13]. We also selected dopaminergic neurons
69 (DNs) from the ventral tegmental area of the midbrain (VTA), which are normally
70 quiescent but are activated during cue-guided reward-based learning[14]. Finally, we
71 compared GAM data from the selected brain cell types to publicly available
72 multiplexGAM data from mESCs[9] (see **Methods, Supplemental Table 1**).
73
74 Tissues were collected from fixative-perfused animals, cryoprotected by
75 sucrose embedding, and then frozen in liquid nitrogen (**Fig. 1b**). After cryosectioning
76 into ~230 nm thin tissue slices, the brain cells of interest were immunostained with
77 specific antibodies. For each GAM sample from single animals, we collected nuclear
78 slices from single cells, by laser microdissection. Next, the DNA content of each

79 sample (containing three nuclear slices) was extracted, amplified and sequenced
80 (627-1755 cells passed QC; **Table 1**). A detailed flowchart of the data collection and
81 quality control measures are presented in **Extended Data Fig. 1a-c, and**
82 **Supplemental Table 2**. We selected a working resolution of 50 kb, based on good
83 sampling of pair-wise co-segregated loci across all datasets; mappable intra-
84 chromosomal locus pairs are detected an average of 7-10 times within 10 Mb
85 (**Extended Data Fig. 1d**), and 98.8-99.9% are found at least once at all genomic
86 distances (**Table 1**).
87
88 ***ImmunoGAM detects 3D chromatin contacts of specific brain cell types***
89 To explore differences in chromatin contacts for each cell type and biological
90 replicate, we produced normalized chromatin contact matrices which inform about
91 inter-locus 3D physical distances[3]. Visual inspection of contact matrices shows clear
92 differences in pairwise contacts between all four cell types, with PGNs and DNs
93 having the highest similarity, which is recapitulated in the biological replicates (**Fig.**
94 **1c**). For example, cell-type specific 3D genome topologies are observed across a 5-
95 Mb region centered on the *Htr1a* gene, which encodes the 5-hydroxytryptamine
96 (serotonin) receptor 1A. HTR1A modulates synaptic transmission in the
97 hippocampus, and has single-nucleotide polymorphisms (SNPs) associated with
98 schizophrenia[15]. *Htr1a* is not expressed in mESCs nor in OLGs, and is embedded in
99 strongly interacting domains that have different conformations in DNs and in PGNs
100 (**Fig. 1c**). An additional example on chromosome 17 shows strong contact patches
101 that span 35 Mb in the three brain cell types but not in the mESCs (**Fig. 1d**), and
102 which are reproduced in the biological replicates (**Extended Data Fig. 1e**). Thus,
103 immunoGAM reveals extensive short- and long-range rearrangements of the 3D
104 chromatin architecture in neurons and OLGs in the adult mouse brain.

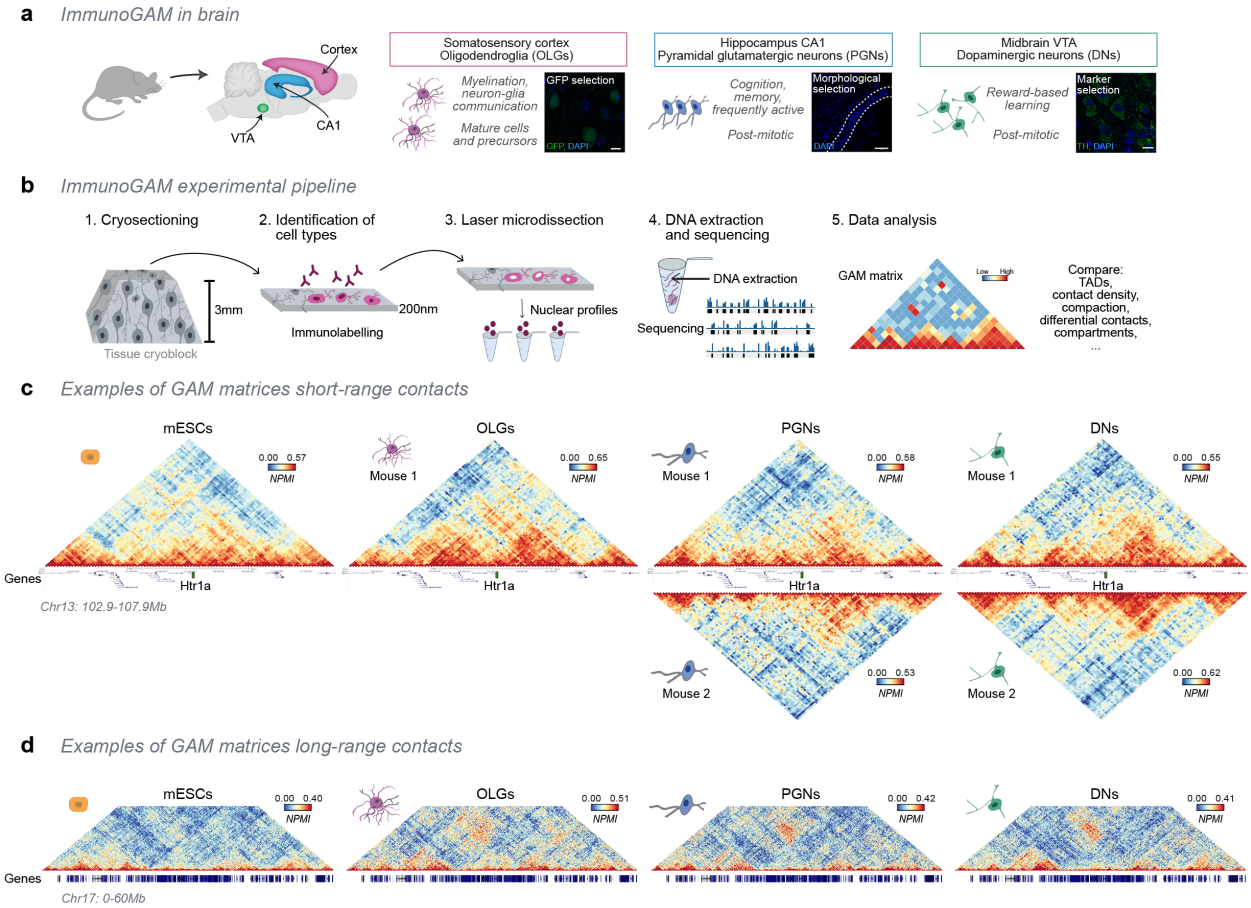

Figure 1. ImmunoGAM captures cell-type specific chromatin contacts in the mouse brain.

a, Immuno-GAM was applied to oligodendrocytes (OLGs), pyramidal glutamatergic neurons (PGNs), and dopaminergic neurons (DNs) (scale: 10, 100 and 10 µm, respectively). OLGs were selected based on GFP expression, PGNs using tissue morphology (dotted line), and DNs by TH expression.

b, The immunoGAM experimental workflow. Upon transcardial perfusion with fixative, brain tissues are dissected, cryoprotected, and ultrathin cryosectioned (1). After immunodetection using cell-type specific markers (2), single nuclear profiles are laser microdissected (3), each from a single cell, and collected in groups of three, as described for multiplex-GAM[9]. After extraction of genomic DNA and sequencing (4), the frequency of co-segregation of pairs of genomic loci is used to calculate matrices of pairwise contacts, and to compare the organization of topological domains, chromatin compaction, differential contacts, and compartments (5).

c, Examples of contact matrices showing cell-type specific differences in local contacts within a 5-Mb genomic region centered on the *Htr1a* gene, which encodes 5-hydroxytryptamine (serotonin) receptor 1A, in mESCs, OLGs, PGNs and DNs. GAM matrices represent co-segregation frequencies of pairs of 50-kb genomic windows using normalized pointwise mutual information (NPMI). Contact maps show reproducible chromatin folding in replicate data collected from single animals for PGNs and DNs.

d, Exemplar of cell-type specific differences in long-range contacts within a 60-Mb genomic region in chromosome 17. Patches of strong contacts involving two large genomic regions separated by ~35 Mb are observed in brain cells, but not in mESCs.

132 ***Topological domains have cell-type specific boundaries that contain cell***
133 ***specialization genes***

134 To investigate cell-type specific 3D genome topologies and how they relate
135 with gene expression, we analyzed published single-cell transcriptomes from the
136 cortex, hippocampus and midbrain after identifying the populations of cells equivalent
137 to the brain cell types captured by immuno-GAM. We selected eight subtypes of
138 mature OLGs and OLG progenitors[16], three subtypes of PGNs from CA1[17] and four
139 DN subtypes from the VTA[18] (**Extended Data Fig. 2a**). We also generated single cell
140 transcriptome data from mESCs and showed that it correlates with published bulk
141 RNA-seq data[19](**Extended Data Fig. 2a-b**). Separation of the different
142 transcriptomes into cell-type specific clusters was confirmed by Uniform Manifold
143 Approximation and Projection (UMAP) dimensionality reduction, and validated by
144 overlaying the expression of known cell-type marker genes (**Extended Data Fig. 2c-**
145 **d**). Next, we produced pseudobulk expression datasets for each cell type by pooling
146 single-cell transcriptomes. A threshold of regularized log (R-log) ≥2.5 was used to
147 designate expressed genes (see **Methods**, **Extended Data Fig**. **2e**). Examples of
148 expression profiles for known marker genes for each cell type are shown in
149 **Extended Data Fig. 2f.**
150

151 Next, we mapped the organization of topologically associating domains
152 (TADs) in the four cell types, using the insulation score method[3,20]. Extensive
153 reorganization of TADs was found across the genome, for example, at the *Gabr* gene
154 cluster, encoding GABA receptors which are not expressed in mESCs and are most
155 active in PGNs, especially *Gabra2* and *Gabrb1* (**Fig. 2a**), and at the *Hist1* locus
156 which contains clusters of replication-dependent histone-1 genes highly expressed in
157 mESCs (**Extended Data Fig. 3a**). We find that TADs have similar average lengths (~

158 1Mb; **Extended Data Fig. 3b**), but their genomic positions vary extensively between
159 cell types (**Fig**. **2b** shows the top seven combinations; for all combinations see
160 **Extended Data Fig**. **3c**). One third of all TAD borders are unique to one cell type (7-
161 10% for each cell type), 8% are shared between the three brain cell types, but only
162 14% are common to all cell types (for example, only 29% of mESC TAD borders are
163 found in the other brain cell types; **Fig**. **2b**). The two neuronal cell types show only
164 35% conservation between TAD borders, in contrast with 59-65% conservation
165 between their biological replicates (**Extended Data Fig. 3c-d**). We also find that TAD
166 boundaries common to all cell types show stronger insulation in the brain cell types
167 than mESCs, possibly reflecting structural domain stabilization upon terminal
168 differentiation (**Fig. 2c**). In contrast, cell-type specific boundaries are less insulated,
169 except for the borders that contain expressed genes in each brain cell type.
170
171 Next, we asked whether the rewired TAD boundaries contained cell type-
172 specific genes. Genes found at unique TAD boundaries are enriched for gene
173 ontology (GO) terms relevant for the specialized functions of each cell type (**Fig. 2d**).
174 mESC-specific boundaries are enriched for genes associated with 'nucleosome
175 activity' (e.g. *Hist1* locus), and 'anterior/posterior pattern specification' (e.g. *Hoxa*
176 genes involved in embryonic development[21]). Boundaries unique to OLGs are
177 enriched for genes involved in 'cell cycle arrest', which relates with the recent
178 terminal differentiation of many OLGs, 'synapse organization', including genes that
179 encode synaptic proteins and neurotransmitter receptors expressed in OLGs, and
180 with functions in the response to neuronal input and modulation of myelin formation[22].
181 PGN-specific TAD borders also contain cell specialization-related genes, with roles in
182 'membrane depolarization' and 'cognition', including the modulation of the response

183 to neuronal activation[23]. DN-specific borders contain genes related to neuronal

184 development, and notably ‘protein tyrosine phosphatase activity’, important for

185 dopaminergic differentiation, regulation of tyrosine hydroxylase activity and dopamine

186

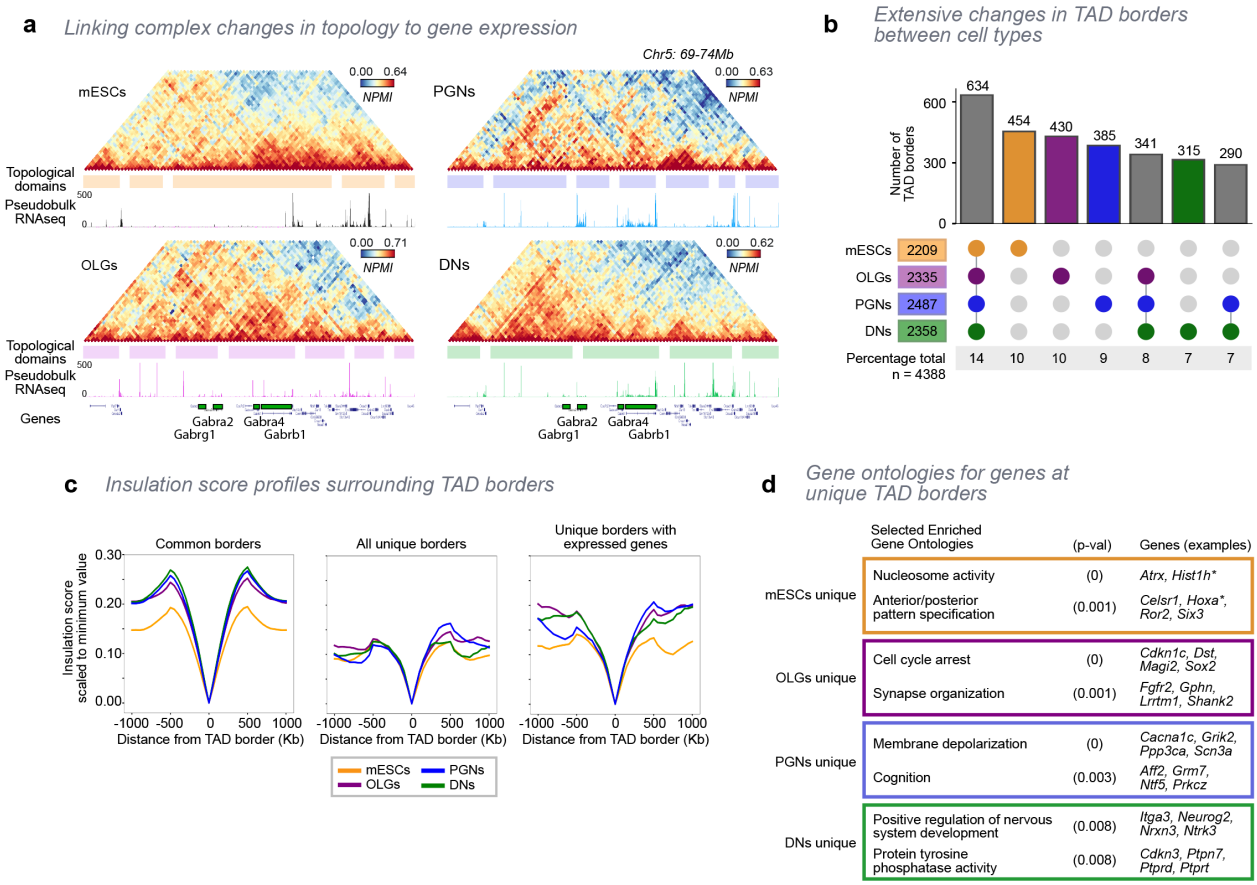

187

188 **Figure 2. Extensive reorganization of topological domains in specialized cells of the**
189 **brain.**

190 **a**, GAM contact matrices show cell-type specific differences in local contacts and topological
191 domains within a 5-Mb region containing a cluster of GABA receptors (50-kb resolution).
192 Shaded regions indicate topological domains. Mouse replicate 1 is shown for brain cells.

193 **b**, Only 634 (14%) of borders are common to all cell types, followed by ~315-454 borders
194 that are cell-type specific. The top seven combinations are shown (for all combinations see
195 **Extended Data Fig. 3c**). TAD boundaries were defined as 150-kb genomic regions centered
196 on lowest insulation score window.

197 **c**, Average insulation score profiles of common or unique borders centered on the lowest
198 insulation point within each TAD border. Common TAD borders are more insulated in brain
199 cell types than mESCs (*left*). Unique borders have similar boundary strength across cell
200 types (*center*). Unique borders containing expressed genes are stronger in brain cell types
201 than in mESCs (*right*).

202 **d**, Selected gene ontologies for genes found at unique TAD borders. For all cell types, genes
203 at unique TAD borders have enriched ontologies relevant for their cell functions (permuted p-
204 values <0.05, 2000 permutations; Z-Score >1.96).

205

206 synthesis, and G-protein coupled receptor mediation of dopaminergic cell
207 signalling[24,25]. We overlapped expressed genes with cell-type specific TAD
208 boundaries, and found that 38% of mESC-specific TAD boundaries contain mESC
209 expressed genes, while 52-55% of boundaries specific to the brain cell types contain
210 expressed genes respective to each cell type (**Extended Data Fig. 3e**). Our results
211 show that the mapping of TADs in pure populations of terminally-differentiated cells
212 detects a previously unappreciated variation in TAD organization, which is strongly
213 connected with the presence of cell-type specific genes at TAD borders.
214

215 ***Extensive reorganization and loss of contact density of the Neurexin-3 gene in***
216 ***DNs***

217 Many neuronal genes which are involved in specialized cell processes, such
218 as synaptic plasticity, often are longer than 250kb, contain several alternative
219 promoters, and produce many isoforms due to alternative initiation sites and complex
220 RNA processing[26]. The regulation of long genes is especially important for neuronal
221 function, as their disruption or the presence of SNPs have been identified in
222 neurodevelopmental or degenerative disorders[27,28]. Transcription of many long
223 neuronal genes is also sensitive to topoisomerase inhibition suggesting their
224 expression is highly dependent on topological constraints[29]. Neurexin-3 (*Nrxn3*) is a
225 1.54Mb long gene highly affected by topoisomerase inhibition. *Nrxn3* encodes a
226 membrane protein involved in synaptic connections and plasticity, and for which
227 genetic variation is associated with alcohol dependence and autism spectrum
228 disorder[27,30]. In mESCs, *Nrxn3* spans two TADs and with an almost undetectable
229 expression level (**Fig. 3a, Extended Data Fig. 4a**). *Nrxn3* is increasingly expressed
230 in OLGs, PGNs and DNs. Remarkably, we found a general loss of TAD contact

density throughout the *Nrxn3* gene in DNs, especially in the second TAD, a phenomenon that we report here as 'TAD melting'.

To compare the changes in contact densities between cell types, we visualized the heatmap of a range of insulation scores (**Fig. 3b**). We found strong contact density present in both TADs in mESCs and OLGs although *Nrxn3* has higher expression in OLGs compared to mESCs (R-log = 8 compared with R-log = 3). With further increases of *Nrxn3* gene expression in PGNs (R-log = 9), the contact density became weaker in the first TAD, before extensive loss of contact density in DNs (R-log = 10). Biological replicates in PGNs and DNs confirm the increased levels of melting in DNs (**Extended Data Fig. 4b**).

Modelling the loss of Nrxn3 TAD structure shows decompaction of chromatin

To better understand how the loss of TAD structure could influence 3D chromatin folding, we used a polymer-physics-based approach (PRISMR)[31] to model the 3D structure of the *Nrxn3* region in mESCs and DNs (**Fig. 3c-d**). We generated 3D models from the GAM matrices, which we validated by applying an "*in-silico* GAM" approach[10] to randomly section a single nuclear profile for each model. Reconstructed *in-silico* GAM chromatin contact matrices closely resemble the experimental data for both mESCs (Pearson r = 0.72) and DNs (r = 0.79). Importantly, the loss of contacts in the second *Nrnx3* TAD is captured by the *in-silico* matrices.

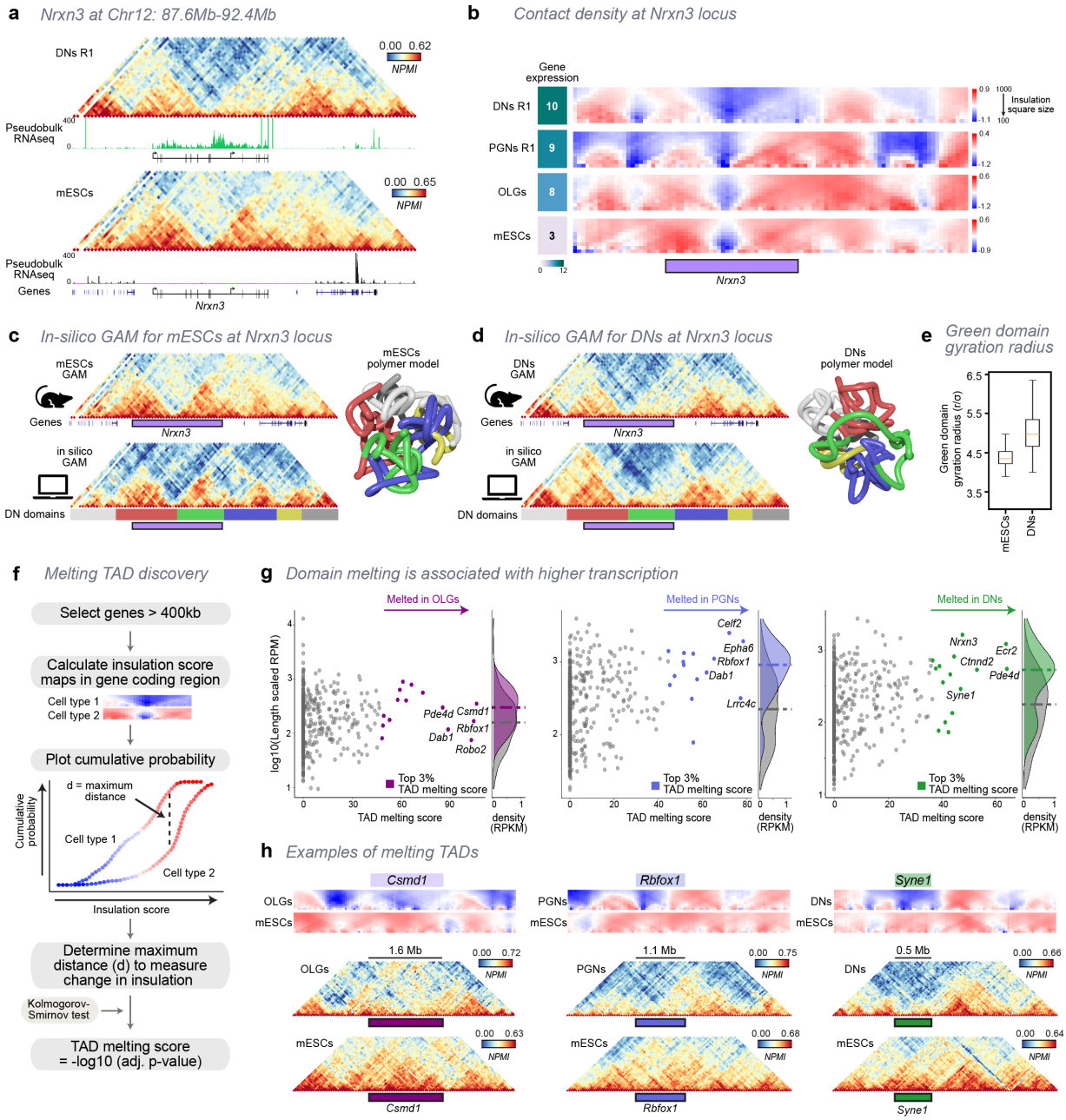

Figure 3. Extensive remodeling of chromatin structure and TAD melting at long and highly expressed genes.

a, GAM contact matrices show the *Nrxn3* locus, a long (1.5Mb) gene which is highly expressed in DNs, but not in mESCs (50-kb resolution; chr12: 87,600,000-92,400,000). *Nrxn3* occupies two TADs with strong contacts in mESCs, which become decondensed, or 'melted' in DNs.

b, Insulation score maps at the *Nrxn3* locus in mESCs, OLGs, PGNs and DNs (square sizes 100 - 1000 kb). *Nrxn3* contact density is strongest for mESCs, becoming increasingly decondensed in OLGs, PGNs and DNs, as its expression increases from R-log equal to 3, 8, 9 and 10, respectively.

c,**d**, Ensembles of polymer models were produced for the *Nrxn3* locus in mESCs (**c**) and in DNs (**d**) from experimental GAM data using PRISMR modelling. The quality of the models was verified by applying in-silico GAM to the ensemble of polymers and comparison between NPMI-normalized contact matrices from in-silico and experimental immunoGAM (Pearson r = 0.72 and 0.79 for mESCs and DNs, respectively). Colour bars below *in-silico* matrices

(Fig. 3 legend, cont.) highlight the position of domains in DNs and are used to colour the polymer examples shown. *Nrxn3* locus polymers have a globular structure with subdomains that interact with one another in mESCs (**c**). In DNs, the second TAD containing the Nrxn3 gene (green domain) becomes extended and loops away (**d**).

e, The second *Nrxn3* TAD (green domain) has higher gyration radii in DNs than mESCs, consistent with its decondensed, melted state in DNs.

f, TAD melting was determined for long expressed genes (>400 kb, 479 genes) from insulation score heatmaps. The distributions of insulation score values were compared between brain cell types and mESCs. The maximum distance between the distributions was determined using one-sided Kolmogorov-Smirnov testing and a TAD melting score was calculated based on the distribution dissimilarity.

g, Genes with the top melting scores have higher RPM values, especially in PGNs and DNs.

h, Examples of genes with top melting scores in each brain cell type.

Next, we inspected single polymer models (**Fig. 3c,d**; coloured according to the structure of domains found in DNs). In the mESC models, the structure of the region was globular and highly intermingled (**Supplemental movie 1**; additional example models for both cell types can be found in **Extended Data Fig. 4c**). The second *Nrxn3* TAD (in green) interacts frequently with the surrounding domains. Remarkably, the second *Nrxn3* TAD is highly extended in DNs (**Supplemental movie 2**). Across the ensemble of DN polymer models, the second *Nrxn3* TAD shows much higher gyration radii compared to the same genomic region in mESCs, indicating that the region tends to be highly decondensed or 'melted' (**Fig**. **3e**). In contrast, the TADs upstream and downstream to *Nrxn3* show marked decreases in gyration radii in DNs, which may be related to changes in gene expression in the neighbouring domains and/or potentially to torsional stress due to extensive *Nrxn3* transcriptional activity (**Extended Data Fig**. **4d**). The loss of contact density and decondensation observed in *Nrxn3* highlights the complicated restructuring of local and long-range chromatin organization for different activation states of long neuronal genes, which can result in loss of the topological structure, decompaction, and melting of entire TADs.

302 ***Genome-wide detection of TAD melting is related with high transcription of***
303 ***long genes***
304 To investigate whether TAD melting occurred in other long genes and in all
305 brain cell types, we devised a pipeline to detect TAD melting based on the
306 differences between cumulative probabilities of insulation scores. We determined a
307 'TAD melting score', as the significance value of the differences between the
308 maximum distances of cumulative probabilities between two cell types **(Fig. 3f**). We
309 calculated TAD melting scores for all genes longer than 400kb and expressed in at
310 least one cell type (479 genes; **Supplemental Table 3**). We found that *Nrxn3* has
311 TAD melting scores of 48 and 49 (replicates 1 and 2, respectively) when comparing
312 DNs to mESCs (**Extended Data Fig. 4e**). We calculated TAD melting scores for all
313 the brain cell types in comparison to mESCs, and explored further the genes with the
314 top 3% of TAD melting scores in each cell type (15 genes in each cell type; **Fig. 3g;**
315 **Extended Data Fig. 4f** shows the results for PGN and DN biological replicates).
316
317 To investigate whether TAD melting is generally related with transcriptional
318 activity, we compared melting scores to the length-normalized number of reads
319 covering both exons and introns (length-scaled Reads per Million; RPM; see
320 **Methods**). Calculating transcriptional activity over the whole gene body allowed us to
321 capture intronic reads which were abundantly detected in many long genes, for
322 example at the *Nrxn3* gene in DNs (**Fig. 3a**). We find that the highest melting scores
323 are associated with highest transcription in all three brain cell types, most
324 pronounced in PGNs and DNs (**Fig. 3g**). Remarkably, 55% of all genes with top
325 melting scores in any cell type or replicate (24 of 44 genes) were previously found to
326 be sensitive to topoisomerase inhibition[29], compared to only 16% of the other genes
327 tested (69 of 435; Fisher's exact p-value = $4x10^{-8}$; **Extended Data Fig**. **4g**).

328 Examples of several genes with the highest melting scores are shown in **Fig.**
329 **3h** (see **Extended Data Fig. 4h** for cumulative probability scores). In OLGs, the top
330 melting score was found for *Csmd1*, which is sensitive to topoisomerase inhibition[29]
331 and a multiple sclerosis[32] and schizophrenia risk gene[33]. In PGNs, *Rbfox1* is a top
332 melting gene, also sensitive to topoisomerase inhibition, with mutations linked to
333 epilepsy and autism spectrum disorder[34,35]. In DNs, another example includes *Syne1*,
334 with mutations leading to muscular dystrophy and Parkinsonian-like symptoms[36].
335 Together, these observations highlight that TAD melting is an appreciated topological
336 feature robustly captured by immunoGAM, which occurs at very long genes, often
337 when these genes have the highest expression levels.
338
339 ***Cell-type specific chromatin contacts contain binding motifs of differentially***
340 ***expressed transcription factors***
341 To explore whether the extensive rearrangements in chromatin topology found
342 in specialized brain cells are related with changes in the landscape of cis-regulatory
343 elements, we investigated in detail the differences in specific chromatin contacts for
344 PGNs and DNs, and whether they contain putative binding sites for neuronal specific
345 transcription factors (TFs). First, we determined differential chromatin contacts by
346 extracting the top 5% cell-type specific contacts below 10Mb (**Fig. 4a**). We identified
347 locations of TF binding motifs for 218 TFs expressed in PGNs and/or DNs. To restrict
348 the search space within the 50-kb windows, we collected open chromatin regions
349 from published scATAC-seq experiments in PGNs[37] and from single-cell low-input
350 chromatin accessibility (liDNAse-seq) peaks in DNs[38]. Next, we selected TFs that are
351 differentially expressed in PGNs and DNs and with motifs present in at least 5% of
352 differential windows, finding 16 DN-specific TFs and 32 PGN-specific TFs (**Extended**
353 **Data Fig. 5a-d**). We searched for pairs of windows with TF motifs (across the 1176

354 possible pairwise TF combinations) that were most enriched in one or the other cell
355 type, or with a high ability to distinguish contacts between each cell type (see
356 **Extended Data Fig. 5e** for full pipeline and criteria). Twenty TF motif pairs were
357 considered for further analysis, containing combinations of 14 of the initial 48 TF
358 motifs considered (**Extended Data Fig. 6a**, see **Supplemental Table 4** for all TF
359 pairs).
360
361 We next searched for the overlap between TF motifs in the same pairs of
362 contacting windows (**Fig. 4b**). The most frequent pair of TF motifs in both cell types is
363 *Maz-Nr3c1* (2732 and 2241 contacts in PGNs and DNs, respectively) which involves
364 *Maz* (which targets NMDA receptor genes[39]) in one contact anchor, and *Nr3c1*
365 (associated with depression and anxiety disorders[40]) in the other anchor (**Fig. 4b,**
366 **Extended Data Fig. 6b**). In PGNs, the next five groups of contacts have multiple TF
367 feature pairs that include *Maz-Nr3c1*, plus combinations of eight different TFs:
368 *Neurod1, Neurod2, Egr1, Etv5, Lhx2, Meis2, Sp3,* and *Ubp1* (*multi-TF* group;
369 combined total of 2363 contacts). In contrast, in DNs, the most abundant group of
370 contacts after *Maz-Nr3c1*, are contacts that do not contain *Maz-Nr3c1*, and have
371 instead *Ctcf-Ctcf* alone (*Ctcf-Ctcf* group; 1277 contacts) or multiple groups of *Ctcf*
372 heterotypic contacts with *Foxa1*, *Nr2f1* or *Nr4a1* (*Ctcf-TF* group; combined total of
373 4343 contacts). The significant contacts in all groups are found across all genomic
374 distances considered (50kb-10Mb) though slightly enriched at >3Mb (**Extended Data**
375 **Fig. 6c**). In light of the association between CTCF and TAD borders[41], we checked
376 whether contacts overlap with TAD borders. We find that only ~25-35% of contacts
377 involve a TAD border, except for *Ctcf-Ctcf* contacts in DNs, of which 47% involve a
378 TAD border (11% involve a TAD border at both windows; range of contact distances
379 is 50kb-2Mb; **Extended Data Fig. 6d**).

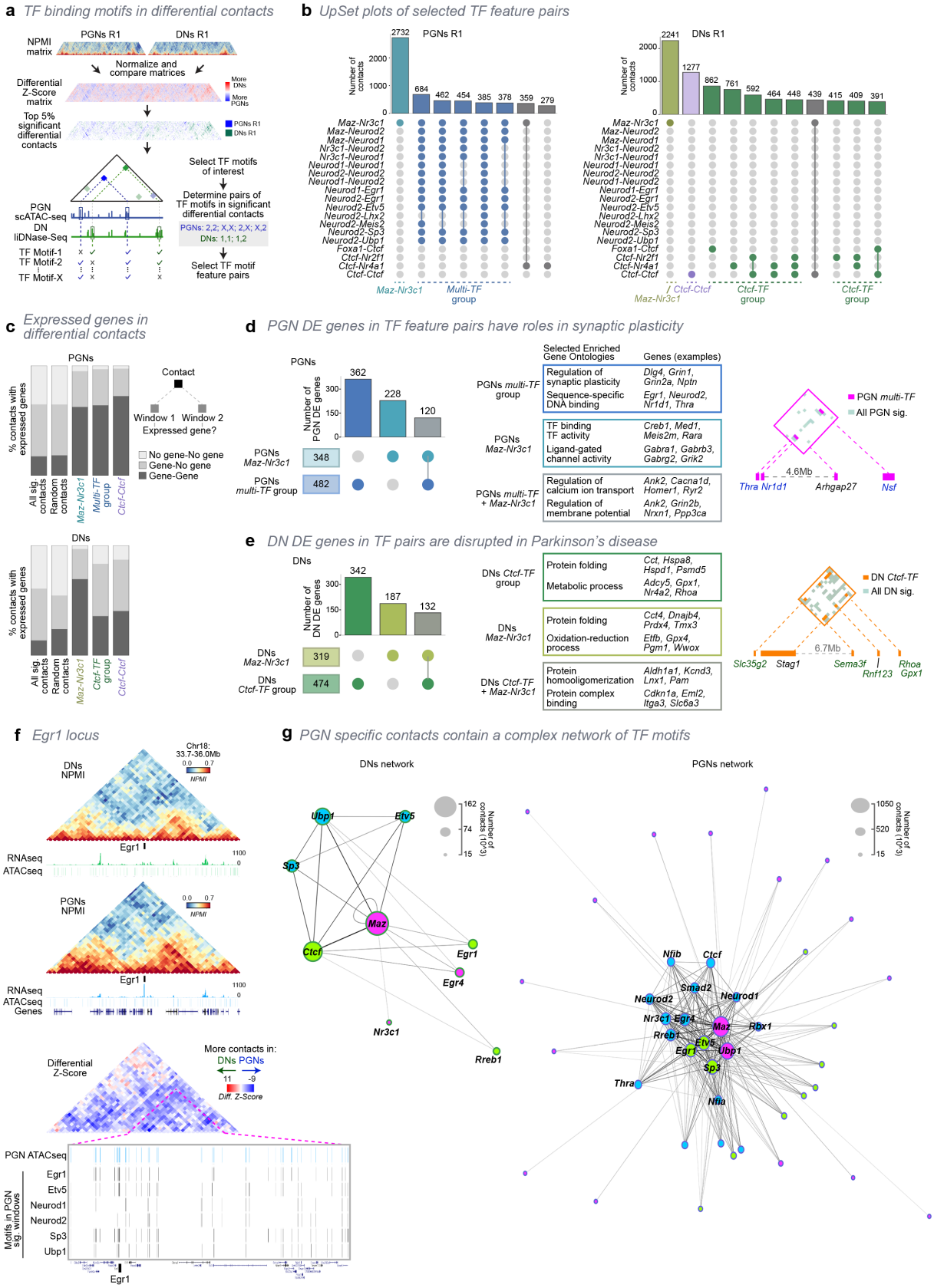

Figure 4. Neuron-specific genes establish PGN- and DN-specific contacts, which contain rich networks of TF binding sites within accessible regions.

a, GAM contacts from PGNs and DNs were normalized and subtracted to produce a matrix of cell-type differential contacts (differential Z-Score matrix). The top 5% differential contacts for PGNs or DNs within 10 Mb were selected, and overlapped with accessible chromatin

386 *(Fig. 4 legend, cont.)* regions to identify candidate regulatory elements. These accessible
387 elements were used to search for putative binding sites of PGN and DN differentially
388 expressed transcription factors (TFs). The most abundant TF feature pairs (top 20) were
389 further investigated. R1, mouse replicate 1.
390 **b**, Multiple TF feature pairs coincide in the same PGN (*left*) or DN (*right)* differential contacts.
391 The top groups of contacts are shown for each cell type.
392 **c**, Differential contacts with the most enriched TF feature pairs in PGNs and DNs contain
393 expressed genes in at least one contacting window, often in both.
394 **d**, Differential contacts involving the most abundant TF feature pairs in PGNs contain
395 differentially expressed genes with PGN-specific roles. (*Right*) Matrix shows differential
396 contacts established between PGN upregulated genes. Gene names highlighted in blue are
397 upregulated in PGNs.
398 **e**, Differential contacts containing the most abundant TF feature pairs in DNs also contain
399 differentially expressed genes with roles in DN-specific functions. (*Right*) Matrix shows
400 contacts between DN upregulated genes. Gene names highlighted in green are upregulated
401 in DNs.
402 **f**, In DNs, the *Egr1* gene establishes weak contacts with a large downstream domain. In
403 PGNs, *Egr1* is upregulated and shows stronger interactions within the downstream domain.
404 The differential contact (Z-Score) matrix shows increased PGN-specific contacts in the whole
405 region surrounding *Egr1*. The *Egr1*-containing TAD has multiple TF binding sites found within
406 PGN accessible regions.
407 **g**, Network analysis and community detection for TF motifs found within DN or PGN
408 differential contacts.
409

410 ***Cell-type specific chromatin contacts contain differentially expressed genes***

411 Next, we investigated whether the genomic regions involved in cell-type
412 specific contacts connect neuronal genes with their candidate regulatory regions or
413 with other genes, and whether they share neuronal functions. Remarkably, we found
414 that a high percentage of differential contacts within the TF motif groups contain
415 expressed genes in both contacting windows (36-72%, 25-47% in only one window;
416 **Fig. 4c**). Many of these genes are differentially expressed (1609 and 2149 genes, in
417 PGNs and DNs respectively), except for the *Ctcf-Ctcf* group which has the lowest
418 number of differentially expressed genes (**Extended Data Fig. 6e**).
419

420 Many of the differentially expressed TFs with highest coverage in the PGN and
421 DN differential contacts are known to have roles in neuronal activation[42,43], therefore
422 we focused our further analyses on the genes most highly expressed in the cell type
423 where they have stronger contacts. In PGN-specific contacts, the PGN-upregulated

genes are found in the *multi-TF* (362 genes) or *Maz-Nr3c1* (228) contacts, with 120 genes sharing both types of contact (**Fig. 4d**). These genes share GO terms related to synaptic plasticity, the regulation of calcium transport, and TF binding and activity.

Interestingly, several of the genes are themselves TFs with motifs enriched in the PGN-specific contacts, including *Egr1* and *Neurod2*, also involved in the response to neuronal activation and synaptic plasticity[42,43]. Two other genes encoding for PGN-upregulated TFs, *Thra* and *Nr1d1*, are closely located in chromosome 11 (separated by ~3 kb) and establish a hub of *multi-TF* contacts with *Arhgap27* (at 4.6 Mb distance), involved in cognitive function[44], and *Nsf* (5.1 Mb), which binds AMPA receptors and regulates both long-term potentiation (LTP) and depression (LTD; **Extended Data Fig. 6f** shows Z-Score matrix)[45].

DN-upregulated genes are exclusive to either the *Ctcf-TF* (342) or *Maz-Nr3c1* (187) groups, with 132 genes sharing contacts with both groups (**Fig. 4e**). Their GO terms are related to protein folding and metabolic functions, with many proteins in these groups dysregulated in Parkinson's disease (PD) and other neuronal disorders. For example, *Gpx1* and *Rhoa* are both involved in oxidation-reduction reactions and disrupted in PD[46,47], and make *Ctcf-TF* containing contacts with the DN-upregulated genes *Semf3* (involved in neural circuit formation and a PD risk gene[48]), and *Rnf123* (an E3-ubiquitin ligase implicated in major depressive disorder[49]). These four genes form a hub of specific *Ctcf-TF* containing contacts with the schizophrenia risk gene *Slc35g2*[50] and the cohesin subunit *Stag1* (**Extended Data Fig. 6g** shows Z-Score matrix).

449 We explored further *Egr1*, an immediate early gene upregulated in activated
450 neurons[42], which establishes PGN-differential contacts that contain *Egr1* and *multi-*
451 *TF* motifs. In DNs, the *Egr1* gene is expressed (R-log = 6.8), and found at a TAD
452 border with some interactions with its right-sided TAD (**Fig. 4f, Extended Data Fig.**
453 **6h**). In PGNs, where cells are frequently activated[12,13], *Egr1* is highly upregulated (R-
454 log = 9.5) and becomes strongly embedded with the right TAD. In the differential
455 contact matrix, most contacts within the *Egr1*-containing TAD are stronger in PGNs
456 and associated with a high density of ATAC-seq peaks that contain complex
457 combinations of motifs for the TFs found in the group of contacts containing the *Egr1*
458 gene (sixth group in PGNs; **Fig. 4b**), including *Egr1, Etv5*, *Neurod1, Neurod2, Sp3*
459 and *Ubp1*.
460
461 ***PGN-specific contacts contain complex interconnected networks of TF binding***
462 ***sites***
463 To explore the complex overlap of multiple TF motifs observed in the PGN- but
464 not the DN-differential contacts more broadly, we next explored the degree of
465 interconnectivity of TF motifs in differential contacts without pre-selection of the
466 windows containing specific TFs (i.e. across the 1176 possible pairwise combinations
467 of the 48 TFs). We built networks of all 48 TF motifs based on their co-occurrence in
468 the top 5% differential contacts of PGNs or DNs, followed by community detection
469 using the Leiden algorithm (see **Methods**, **Extended Data Fig. 6i, Supplemental**
470 **Table 5**). Each TF motif was a node of the network, and the number of differential
471 contacts between windows containing the motifs were the edges. To detect the
472 strongest patterns, we considered only the TF motifs involved in >15,000. In DNs, we
473 detected three communities with *Maz* as the central motif for one community, which
474 also contained *Nr3c1* and *Egr4* (**Fig. 4g**). *Ctcf* is the central motif in a second

475 community which also containing *Egr1* and *Rreb1*, and *Ubp1* is central for a third
476 community, with *Sp3 and Etv5*. The three communities are inter-connected, with the
477 total number of contacts for each motif ranging from ~15,000-162,000. In striking
478 contrast, the PGN network has a dense core of highly connected TF motifs, with up
479 to ~1,040,000 total contacts for *Maz*, which is also the central motif for one
480 community. Two other communities are detected, with *Egr1* and *Etv5* as central
481 motifs for one community, and several core TF motifs, including *Egr4, Neurod1,*
482 *Neurod2, Rerb1* and *Smad2*, as central in the other community. All three
483 communities were interconnected at the core of the network, while more peripheral
484 TFs interact strongly with the core of its community. Together, these results suggest
485 that chromatin contacts specific for different neuron types contain inter-connected
486 hubs of TF motifs, which describe differentially expressed genes involved in
487 specialized cell functions.
488
489 ***Extensive A/B compartment changes occur between brain cells and mESCs,***
490 ***and relate with changes in gene expression***
491 As a final exploration of chromatin contacts in mESCs and the three brain cell
492 types, we investigated large-scale changes of compartment domains associated with
493 open and closed chromatin by performing principal component analyses (PCA)[3].
494 Visual comparisons of normalized compartment eigenvectors show extensive
495 variation of compartments A and B between mESCs and the three brain cell types
496 (**Fig. 5a**, **Extended Data Fig. 7a**). The compartment eigenvector values are best
497 correlated between biological replicates, next between DNs and PGNs, neurons and
498 OLGs, and least between the different brain cells and mESCs (**Extended Data Fig.**
499 **7b**). A large fraction of windows were in compartment A (40%, 2325 windows) in all
500 cell types, but only 15% of windows share compartment B membership (898

501 windows; **Fig 5b, Extended Data Fig. 7c-d**). The next most abundant group of
502 windows undergo changes between compartments B in mESC to A in all the brain
503 cell types (12%, transition B-mESC → A-brain cells) or between compartment A in
504 mESCs to B in brain cells (7%, B-mESC → A-brain cells). Regardless of the changes
505 in compartment membership, the mean and total genomic lengths occupied by A or B
506 compartments is similar across cell types (**Extended Data Fig. 7e-f**).
507
508 To investigate how compartment changes between mESCs and the brain cell
509 types related to gene expression, we clustered genes found in each type of transition
510 according to their expression in each cell type. We find 335 genes within the regions
511 with transition B-mESC → A-brain cells, which are more strongly expressed in all the
512 brain cell types than in mESCs (**Extended Data Fig. 8a**). These genes share
513 functions between the brain cell types and have enriched GO terms such as
514 "behavior", "regulation of synaptic plasticity" and "gated ion channel activity" (**Fig.
515 5c**). In regions that undergo A-mESC → B-brain cells transitions, we remarkably find
516 that most genes are silent in all cell types (572/715 genes that undergo A-to-B
517 transitions), and only 50 genes are more expressed in mESCs (**Extended Data Fig.
518 8b**). Enriched GO terms for these 50 genes include transcriptional regulation and
519 transcription factor activity, and include many *Zfp* genes, encoding zinc-finger binding
520 proteins with roles in the epigenetic regulation of pluripotency factors, and silencing
521 of active genes during the exit from pluripotency[51].

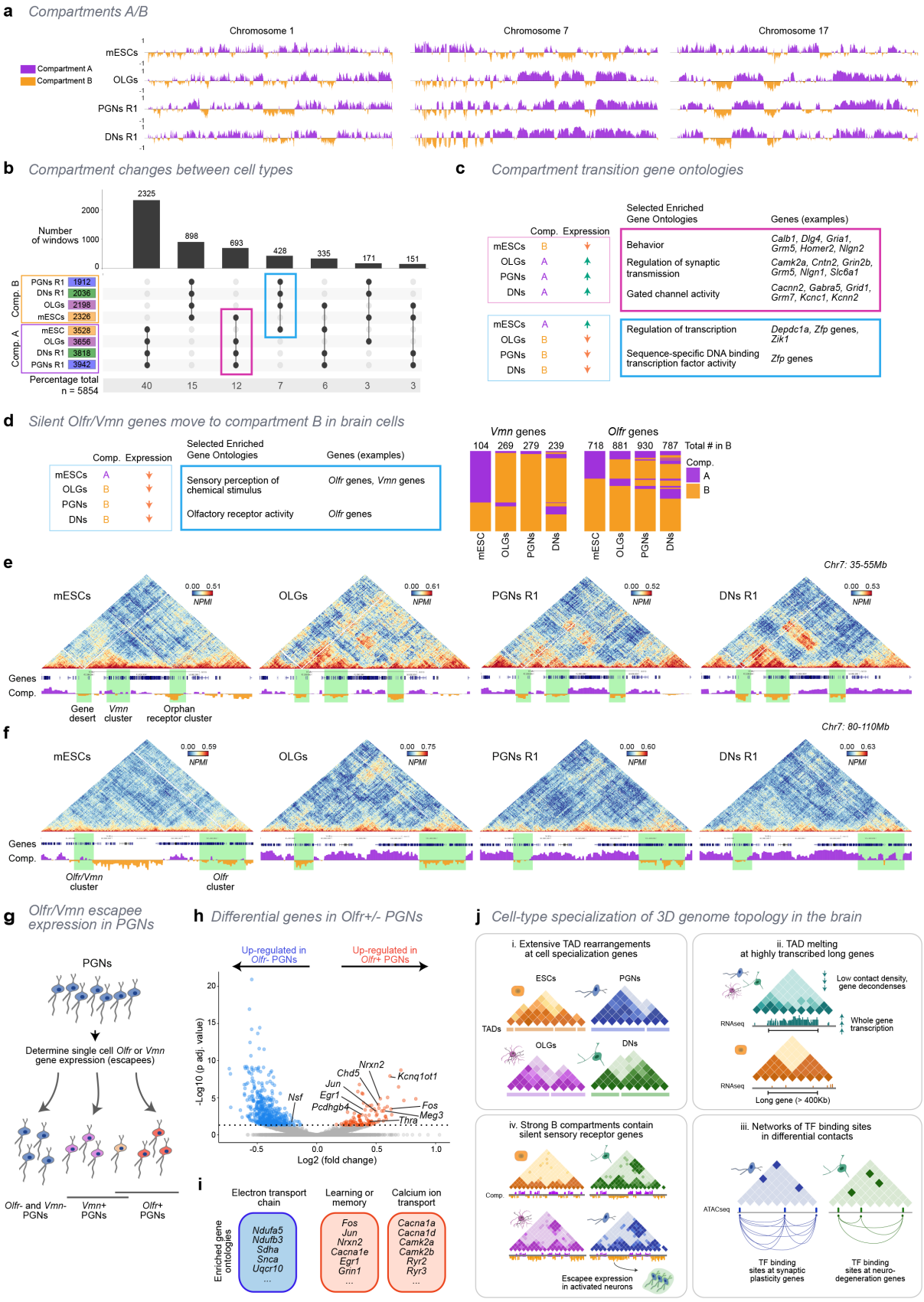

Figure 5. Clusters of sensory receptor genes more often belong to B compartments in brain cells and establish megabase-range interactions.

a, Open and closed chromatin compartments (A and B, respectively) display different genomic distributions in mESCs, OLGs, PGNs and DNs. Normalized PCA eigenvectors were

527 *(Fig. 5 legend, cont.)* computed from GAM datasets from mESCs and for brain cell types,
528 and used to classify compartments. Mouse replicate 1 (R1) is shown for PGNs and DNs.
529 **b**, Most genomic windows share membership to compartments A, followed by B in all cell
530 types. The most frequent compartment changes occur from compartment B in mESCs to A in
531 all brain cells (pink box), followed by from A in mESCs to B in all brain cells (blue box; for all
532 combinations see **Extended Data Fig**. **7d**).
533 **c**, Selected gene ontologies (GOs) for genes that increase expression in all brain cells
534 relative to mESCs and move from compartment B in mESCs to compartment A in brain cells
535 (*pink box*); and for genes that decrease expression in brain cells and move to compartment
536 B, compared to mESCs (*blue box*). All enriched GOs had permuted p-values = 0.
537 **d**, Selected GOs for genes that remain silent in all cell types but gain membership to
538 compartment B in brain cells. Most genes are *Olfr* and *Vmn* sensory receptor cluster genes.
539 A higher proportion of *Olfr* and *Vmn* genes are found in B compartments in brain cells,
540 compared to mESCs. All enriched GOs had permuted p-values = 0.
541 **e**, GAM contact matrices containing *Vmn* and orphan receptor genes shows strong
542 interactions separated by 10 Mb between B compartments in OLGs, PGNs and DNs, but not
543 mESCs. Shaded green regions indicate interacting regions.
544 **f**, GAM contact matrices show interactions between an *Olfr/Vmn* gene cluster and a second
545 *Olfr* cluster (green shaded regions) separated by 25 Mb. The contacts between the two
546 receptor clusters are strongest in OLGs, where the B compartment is strongest.
547 **g**, *Olfr* or *Vmn* escapee expression in single PGN cells. PGN cells were classified as *Olfr*+ or
548 *Vmn*+ if at least one *Olfr* or *Vmn* gene was detected, respectively.
549 **h**, Volcano plot of differentially expressed (DE) genes between Olfr-expressing and non-
550 expressing PGNs. Genes with an adjusted p-value < 0.05 were considered DE.
551 **i**, Selected gene ontologies (GOs) of upregulated genes were enriched for neuronal
552 activation functions, while downregulated genes are involved in mitochondria metabolism.
553 **j**, Summary diagram. The 3D genome is extensively reorganized in brain cells. (i) TAD
554 borders are rearranged, with new border formation coinciding with genes important for cell
555 specialization in all cell types. (ii) TAD melting occurs at very long and highly transcribed
556 genes in brain cells. (iii) The most specific contacts in neurons contain complex networks of
557 binding sites of neuron-specific transcription factors. Contacts bridge genes upregulated in
558 the neurons where the contacts are observed. Genes in contact hubs have functions in
559 synaptic plasticity (PGNs) and neurodegenerative disease (DNs). (iv) Finally, B
560 compartments contain clusters of sensory receptor genes silent in all cell types which form
561 strong megabase-range contacts. A subset of sensory receptor genes escape repression
562 when neurons are activated.
563

564 ***Clusters of sensory receptor genes are more strongly associated with B***

565 ***compartments in brain cells and establish megabase-range interactions***

566 We were intrigued by the large number of genes that undergo A-mESC to B-
567 brain-cell transitions irrespectively of being silent in all cell types. This group of genes
568 contained sensory receptor genes such as *Vmn* (vomeronasal; 149 genes out of 572
569 silent genes in the group) and *Olfr* (olfactory receptor; 179 genes), which are most
570 often found in gene clusters[52,53] (**Fig. 5d**). Although silent in mESCs, only 35% of
571 *Vmn* genes (104/290) and 66% of *Olfr* genes (718/1095) are associated with

572 compartment B, compared to 82-96% and 72-85% in brain cells, respectively (**Fig.**
573 **5d**).
574
575 We explored how the stricter compartment B association of sensory receptors
576 in brain cells was related with chromatin contact formation in regions containing *Vmn*
577 and *Olfr* clusters. Visual inspection of matrices and compartments on chromosome 7
578 (which contains the most *Vmn* and *Olfr* genes combined) showed that *Vmn* genes
579 and/or *Olfr* genes are often involved in strong long-range patches of contacts only
580 observed in brain cells, which can be separated by distances above 10 Mb and up to
581 50 Mb (**Fig**. **5e,f**, **Extended Data Fig. 9a**). For *Olfr* clusters in **Fig. 5f**, the contacts
582 between the two receptor clusters are most clearly found in OLGs, which are strongly
583 within the B compartment. Contacts are also found in PGNs, but not in DNs where
584 the second cluster is in the A compartment. The long-range patches of contacts on
585 chromosome 17 shown in **Fig. 1d** also contain both *Vmn* and *Olfr* genes.
586
587 To investigate the strength of long-range contacts between *Vmn* or *Olfr* genes
588 in non-adjacent compartments, we normalized matrices using Z-Scores at each
589 genomic distance to account for their occurrence at different genomic lengths, and
590 compared the top 20% of Z-Scores at distances >3 Mb. The brain cell types show
591 higher Z-Scores for long-range contacts between B compartment regions containing
592 *Vmn* genes, and to a lesser extent *Olfr* genes, when compared to mESCs or the
593 genome-wide B compartment distribution, with no difference for genes found in
594 compartment A for any cell type (**Extended Data Fig**. **9b**). These results suggest that
595 sensory genes are not only more locally compartmentalized in heterochromatic B
596 compartments, but also form stronger contacts in 3D with other B compartments in
597 brain cells, which suggests a stricter repression mechanism in brain cells.

598 ***PGN subpopulations expressing Olfr genes have gene expression signatures***
599 ***of early neuronal activation***

600 Tighter B compartmentalization of *Vmn* and *Olfr* genes may be important for
601 their repression in the brain cell types. *Olfr* genes have been reported to be
602 stochastically activated, and mis-expressed in several neurodegenerative diseases in
603 cortical PGNs[54]. Additionally, *Olfr* expression significantly increases after
604 pharmacological activation of glutamatergic neuronal firing[7] (**Extended Data Fig.**
605 **9c**), suggesting that some *Olfr* genes can escape repression, dependent on cell
606 state. Taking advantage of the large number of single cell transcriptomes available
607 for PGNs[17], we tested whether single PGNs had any *Olfr* or *Vmn* escapee gene
608 expression (**Fig. 5g,** see **Methods**). We find that 23% (203/876 cells) and 19% (164)
609 of single PGNs have at least one transcribed *Vmn* or *Olfr* gene, respectively.
610

611 To determine whether *Olfr* or *Vmn* escapee expression in PGNs was
612 stochastic or related with functional differences between cell states within the PGN
613 population, we measured differential gene expression between cells expressing at
614 least one *Olfr* (*Olfr*+ PGNs) or *Vmn* (*Vmn*+ PGNs) gene and cells that expressed
615 neither (*Olfr*- or *Vmn*- PGNs). Remarkably, we found 87 genes significantly
616 upregulated in the PGNs expressing at least one *Olfr* gene, and 460 genes which
617 were significantly downregulated (**Fig. 5h, Extended Data Fig**. **9d-e**). In contrast, we
618 found no differentially expressed genes for random subsets of PGNs, and very few
619 between the *Vmn*+ and *Vmn*- PGNs, suggesting their escapee expression is
620 stochastic (**Extended Data Fig. 9f**).
621

622 To further investigate whether the cells with escapee expression of *Olfr* genes
623 might have a specific physiological state, we performed GO analyses of the

624 upregulated genes in *Olfr*-expressing PGNs. Strikingly, and in accordance to the *Olfr*
625 gene expression in neurons upon pharmacological activation[7] (**Extended Data Fig.**
626 **9c**), we found genes related to neuronal activation (**Fig. 5i**). For example, genes
627 involved in the early response to LTP are found in *Olfr*+ PGNs, such as the
628 upregulated genes *Egr1*, *Fos*, *Jun*, *Nrxn2*, and *Grin1*[55], and the downregulated gene
629 *Nsf*[45]. Significantly downregulated genes mostly included mitochondrial related
630 processes, which are coupled to and finely tuned during neuronal activation[55]. Finally,
631 we observed that *Olfr* escapee genes, but not *Vmn* genes, are more likely to escape
632 repression if located in compartment A (**Extended Data Fig. 9g**), suggesting that the
633 tighter B compartmentalization of *Olfr* genes might be important for their repression in
634 brain cell types, especially in PGNs which are undergoing neuronal activation and
635 likely chromatin structure reorganisation[7].
636

637 ***Discussion***

638 Here, we adapted the GAM method to capture genome-wide chromatin
639 conformation states of selected cell populations in the mouse brain that perform
640 specialized functions. Using immunoGAM, we selected nuclear slices from specific
641 brain cells by immunofluorescence prior to laser microdissection, and characterized
642 the relationship between 3D chromatin organization and cell specialization in intact
643 tissues. We discovered dramatic reorganization of chromatin topology which
644 reflected cell function and specialization at multiple genomic scales, from specific
645 contacts to compartment changes that spanned tens of megabases (**Fig. 5j**). For
646 example, we found extensive restructuring of topological domains, with 76% of TAD
647 borders being different in at least one cell type. Unique borders in each cell type
648 contained genes relevant for cell specialization, which may be functionally necessary
649 for their interaction with cis-regulatory elements and transcriptional activation[57].

650 Of particular importance was the observation that the highest expression
651 levels of very long genes in brain cells corresponds with a massive reorganization of
652 local and long-range structure. We show that many highly transcribed long genes
653 lose chromatin contact density, which coincides with the decondensation and
654 unfolding of an entire domain, a phenomenon that we call 'TAD melting'. Many long
655 genes are regulated in a specialized manner in terminally differentiated cells, for
656 example by the activity of topoisomerases[29], by the presence of long stretches of
657 broad H3K27ac and H3K4me1 which act as enhancer-like domains[58], by the
658 formation of large transcription loops[59], or through repressive mechanisms such as
659 DNA methylation[60]. The regulation of long genes is further complicated by intricate
660 splicing dynamics[26], which require highly adaptive responses based on neuronal
661 activation state. In fact, for many of the genes we highlight, including *Nrxn3*, *Csmd1*,
662 *Rbfox1* and *Syne1*, genetic variants are often associated with or directly result in
663 neuronal diseases[27,30,33-36]. Thus, understanding how genome folding relates with the
664 response to environmental challenges is increasingly important to further our
665 understanding of the mechanisms of neurological disease.
666
667 Our results strongly support that prediction of functional or disease states in a
668 cell type could be inferred from chromatin architecture. When we searched for TF
669 binding motifs within accessible regions of specific chromatin contacts for a cell type,
670 we found rich networks of putative binding sites for differentially expressed TFs.
671 These networks connect hubs of differentially expressed genes with specialized
672 functions in neurons. For example, DN-specific contacts contained heterotypic *Ctcf*
673 binding motifs, present in contact hubs containing metabolic and protein folding
674 genes. The accumulation of oxidative damage and disruption of ubiquitin-mediated
675 protein folding are pathological hallmarks of Parkinson's disease[46,47,61]. Therefore,

676 future studies will be important to understand the relationship between DN-specific
677 chromatin landscapes, disease-associated genetic variation and the regulation of
678 these critical genes, with potential implications for the etiology of Parkinson's
679 disease.
680
681 An important contrast found in the PGN-specific contacts was the complexity
682 of TF binding motif networks, which contained hubs differentially expressed genes
683 with roles in synaptic plasticity. PGNs frequently respond to environmental cues
684 during long-term potentiation (LTP) or depression (LTD), either by external stimuli or
685 by stochastic and intrinsic activation[12,13,42,45]. Strikingly, PGN-specific contacts
686 containing TF genes involved in the early activation of LTP such as *Egr1* and
687 *Neurod2*, which were also marked by accessible sites containing their own binding
688 motifs, suggesting mechanisms of self-activation by which expression of a TF
689 increases contacts of the TF with other regions containing its own binding sites.
690 Activity-mediated waves of transcription accompany LTP, from immediate early
691 genes, to secondary response genes, followed by long-term upregulation of synaptic
692 proteins. Further, positive feedback loops of BDNF signaling at local synapses have
693 been proposed as a mechanism of LTP induction[62]. Together with reports that *de*
694 *novo* chromatin looping can accompany transcriptional activation[7], our work suggests
695 that coordinated transcription factor binding at apparent distant locations in the linear
696 genomic scale, but in close contact due to the 3D chromatin landscape, may be
697 critical for LTP induction.
698
699 The interplay of complex architecture and LTP related functions in PGNs was
700 further highlighted by the observed activation of a subset of PGNs with *Olfr*-gene
701 escapee expression. *Olfr* expression escape coincided with immediate early gene

702 and synaptic plasticity-related gene expression. The otherwise tight repression of *Olfr*
703 genes within strong B compartment regions, which form cis-contacts tens of mega-
704 bases away, was especially noteworthy as *Olfr* genes can have non-sensory organ
705 functions in neurons related to specificity of neuronal activation[7,54]. *Olfr* genes are
706 highly repressed in mature olfactory sensory neurons, where they form a large inter-
707 chromosomal hub to regulate specificity of single *Olfr* gene activation[63,64]. Our results
708 expand these previous findings, highlighting that alternative long-range mechanisms
709 of *Olfr* repression may also reflect their specialized roles in different cell types of the
710 brain.
711
712 Finally, our work shows that immunoGAM is uniquely positioned to probe
713 questions related to cell state and specialized function within the brain or in other
714 complex tissues, as local tissue structure is maintained. ImmunoGAM also has the
715 potential to be applied in multiple cell types within the same tissue while retaining the
716 geographic positions of each cell, a prospect that can further deepen our
717 understanding of coordinated interactions between cells in complex diseases. As
718 immunoGAM requires only very small cell numbers to capture complex differences in
719 genomic topology (~1000 cells), it may also have prognostic value in highly precious
720 clinical patient samples, and to provide critical insights into the etiology and
721 progression of neurological disease. Collectively, our work revealed that cell
722 specialization in the brain and chromatin structure are intimately linked at multiple
723 genomic scales.

References

1. Jung, I., *et al.* A compendium of promoter-centered long-range chromatin interactions in the human genome. *Nat. Genet.* **51**, 1442-1449 (2019).

2. Rao, S.S., *et al.* A 3D map of the human genome at kilobase resolution reveals principles of chromatin looping. *Cell* **159**, 1665-1680 (2014).

3. Beagrie, R.A., *et al.* Complex multi-enhancer contacts captured by genome architecture mapping. *Nature* **543**, 519-524 (2017).

4. Quinodoz, S.A., *et al.* Higher-Order Inter-chromosomal Hubs Shape 3D Genome Organization in the Nucleus. *Cell* **174**, 744-757 (2018).

5. Dixon, J.R., *et al.* Chromatin architecture reorganization during stem cell differentiation. *Nature* **518**, 331-336 (2015).

6. Fraser, J., *et al.* Hierarchical folding and reorganization of chromosomes are linked to transcriptional changes in cellular differentiation. *Mol. Syst. Biol.* **11**, 852 (2015).

7. Beagan, J.A., *et al*. Three-dimensional genome restructuring across timescales of activity-induced neuronal gene expression. *Nat. Neurosci.* **23**, 707-717 (2020).

8. Bonev, B., *et al.* Multiscale 3D Genome Rewiring during Mouse Neural Development. *Cell* **171**, 557-572 (2017).

9. Beagrie, R.A., *et al.* Multiplex-GAM: genome-wide identification of chromatin contacts yields insights not captured by Hi-C. Preprint at *BioRxiv* https://doi.org/10.1101/2020.07.31.230284 (2020).

10. Fiorillo, L., *et al.* Comparison of the Hi-C, GAM and SPRITE methods by use of polymer models of chromatin. Preprint at *BioRxiv* https://doi.org/10.1101/2020.04.24.059915 (2020).

11. Huges, E.G., Orthmann-Murphy, J.L., Langseth, A.J., & Bergles, D.E. Myelin remodeling through experience-dependent oligodendrogenesis in the adult somatosensory cortex. *Nat. Neurosci.* **21**, 696-706 (2018).

12. Stackman Jr., R.W., Cohen, S.J., Lora, J.C., & Rios, L.M. Temporal inactivation reveals that the CA1 region of the mouse dorsal hippocampus plays an equivalent role in the retrieval of long-term object memory and spatial memory. *Neurobiol. Learn. Mem.* **133**, 118-128 (2016).

13. Combe, C.L., Canavier, C.C., & Gasparini, S. Intrinsic Mechanisms of Frequency Selectivity in the Proximal Dendrites of CA1 Pyramidal Neurons. *J. Neurosci.* **38**, 8110-8127 (2018).

14. Keiflin, R., Pribut, H.J., Shah, N.B., & Janak, P.H. Ventral Tegmental Dopamine Neurons Participate in Reward Identity Predictions. *Curr. Biol.* **29**, 92-103 (2018).

15. Guan, F., *et al.* Evaluation of association of common variants in HTR1A and HTR5A with schizophrenia and executive function. *Sci. Rep.* **6**, 38048 (2016).

16. Marques, S., *et al.* Oligodendrocyte heterogeneity in the mouse juvenile and adult central nervous system. *Science* **352**, 1326-1329 (2016).

17. Zeisel, A., *et al.* Brain structure. Cell types in the mouse cortex and hippocampus revealed by single-cell RNA-seq. *Science* **347**, 1138-142 (2015).

18. La Manno, G., *et al.* Molecular Diversity of Midbrain Development in Mouse, Human, and Stem Cells. *Cell* **167**, 566-580 (2016).

19. Ferrai, C., et al. RNA polymerase II primes Polycomb-repressed developmental genes throughout terminal neuronal differentiation. *Mol. Syst. Biol.* **13**, 946 (2017).

20. Crane, E., *et al.* Condensin-Driven Remodeling of X-Chromosome Topology during Dosage Compensation. *Nature* **523**, 240-244 (2015).

21. Jerković, I., *et al*. Genome-Wide Binding of Posterior HOXA/D Transcription Factors Reveals Subgrouping and Association with CTCF. *PLoS Genet.* **13**, e1006567 (2017).

22. Shi, R., *et al.* Shank Proteins Differentially Regulate Synaptic Transmission. *eNeuro.* **4**, ENEURO.0163-15.2017 (2017).

23. Petrovic, M.M., *et al.* Metabotropic action of postsynaptic kainate receptors triggers hippocampal long-term potentiation. *Nature Neurosci.* **20**, 529-529 (2017).

24. Zhang, D., *et al.* Protein kinase C delta negatively regulates tyrosine hydroxylase activity and dopamine synthesis by enhancing protein phosphatase-2A activity in dopaminergic neurons. *J. Neurosci.* **16**, 5349-5362 (2007).

25. Xu, Y., & Fisher, G.J. Receptor type protein tyrosine phosphatases (RPTPs) – roles in signal transduction and human disease. *J. Cell Commun. Signal.* **6**, 125-138 (2012).

26. Ray, T.A., *et al.* Comprehensive identification of mRNA isoforms reveals the diversity of neural cell-surface molecules with roles in retinal development and disease. *Nat. Commun.* **11**, 3328 (2020).

27. Vaags, A.K., *et al.* Rare Deletions at the Neurexin 3 Locus in Autism Spectrum Disorder. *Am. J. Hum. Genet.* **90**, 133-141 (2012).

28. Martinez-Mir, A., *et al.* Genetic study of neurexin and neuroligin genes in Alzheimer's disease. *J. Alzheimers Dis.* **35**, 403-412 (2013).

29. King, I.F., *et al.* Topoisomerases facilitate transcription of long genes linked to autism. *Nature* **501**, 58-62 (2013).

30. Hishimoto, A., *et al*. Neurexin 3 polymorphisms are associated with alcohol dependence and altered expression of specific isoforms. *Hum. Mol. Genet.* **16**, 2880-2891 (2007).

31. Bianco, S., *et al.* Polymer physics predicts the effects of structural variants on chromatin architecture. *Nat Genet.* **50**, 662-667 (2018).

32. Baranzini, S.E., *et al.* Genome-wide association analysis of susceptibility and clinical phenotype in multiple sclerosis. *Hum. Mol. Genet.* **18**, 767-778 (2009).

33. Steen, V.M., *et al.* Neuropsychological deficits in mice depleted of the schizophrenia susceptibility gene CSMD1. *PLoS One* **8**, e79501 (2013).

34. Lee, J-A., *et al.* Cytoplasmic Rbfox1 regulates the expression of synaptic and autism-related genes. *Neuron* **89**, 113-128 (2016).

35. Lal, D., *et al.* Extending the phenotypic spectrum of RBFOX1 deletions: Sporadic focal epilepsy. *Epilepsia* **56**, e129-133 (2015).

36. Synofzik, M., *et al.* SYNE1 ataxia is a common recessive ataxia with major non-cerebellar features: a large multi-centre study. *Brain* **139**, 1378-1393 (2016).

37. Sinnamon, J.R., *et al.* The accessible chromatin landscape of the murine hippocampus at single-cell resolution. *Genome Res.* **29**, 857-869 (2019).

38. Tuesta, L.M., *et al.* In vivo nuclear capture and molecular profiling identifies Gmeb1 as a transcriptional regulator essential for dopamine neuron function. *Nat. Commun.* **10**, 2508 (2019).

39. Okamoto, S., Sherman, K., Bai, G., & Lipton, S.A. Effect of the ubiquitous transcription factors, SP1 and MAZ, on NMDA receptor subunit type 1 (NR1) expression during neuronal differentiation. *Brain Res. Mol. Brain Res.* **107**, 89-96 (2002).

40. Boyle, M.P., *et al.* Acquired deficit of forebrain glucocorticoid receptor produces depression-like changes in adrenal axis regulation and behavior. *Proc. Natl. Acad. Sci. U.S.A.* **102**, 473-478 (2005).

41. Barrington, C., *et al.* Enhancer accessibility and CTCF occupancy underlie asymmetric TAD architecture and cell type specific genome topology. *Nat. Commun.* **10**, 2908 (2019).

42. Duclot, F., & Kabbaj, M. The Role of Early Growth Response 1 (EGR1) in Brain Plasticity and Neuropsychiatric Disorders. *Front. Behav. Neurosci.* **11**, 35 (2017).

43. Wilke, S.A., *et al.* NeuroD2 regulates the development of hippocampal mossy fiber synapses. *Neural Dev.* **7**, 9 (2012).

44. Trampush, J.W., *et al.* GWAS meta-analysis reveals novel loci and genetic correlates for general cognitive function: a report from the COGENT consortium. *Mol. Psychiatry* **22**, 336-345 (2017).

45. Lüthi, A., *et al.* Hippocampal LTD Expression Involves a Pool of AMPARs Regulated by the NSF–GluR2 Interaction. *Neuron* **24**, 389-399 (1999).

46. Bogetofte, H., *et al.* Perturbations in RhoA signalling cause altered migration and impaired neuritogenesis in human iPSC-derived neural cells with PARK2 mutation. *Neurobiol. Dis.* **132**, 104581 (2019).

47. Bai, X., *et al.* Neurochemical and motor changes in mice with combined mutations linked to Parkinson's disease. *Pathobiol. Aging Age Relat. Dis.* **7**, 1267855 (2017).

48. Zhang, M., *et al.* Genome-wide pathway-based association analysis identifies risk pathways associated with Parkinson's disease. *Neuroscience* **340**, 398-410 (2017).

49. Teyssier, J-R., *et al.* Correlative gene expression pattern linking RNF123 to cellular stress-senescence genes in patients with depressive disorder: implication of DRD1 in the cerebral cortex. *J. Affect. Disord.* **151**, 432-438 (2013).

50. Thyme, S.B., *et al.* Phenotypic Landscape of Schizophrenia-Associated Genes Defines Candidates and Their Shared Functions. *Cell* **177**, 478-491 (2019).

51. Kwak, S., *et al.* Zinc finger proteins orchestrate active gene silencing during embryonic stem cell differentiation. *Nucleic Acids Res.* **46**, 6592-6607 (2018).

52. Magklara, A., *et al.* An epigenetic signature for monoallelic olfactory receptor expression. *Cell* **145**, 555-570 (2011).

53. Kambere, M.B. & Lane, R.P. Co-regulation of a large and rapidly evolving repertoire of odorant receptor genes. *BMC Neurosci.* **8 Suppl 3**, S2 (2007).

54. Ansoleaga, B., *et al.* Dysregulation of brain olfactory and taste receptors in AD, PSP and CJD, and AD-related model. *Neuroscience* **248**, 369-382 (2013).

55. Minatohara, K., Akiyoshi, M. & Okuno, H. Role of Immediate-Early Genes in Synaptic Plasticity and Neuronal Ensembles Underlying the Memory Trace. *Front. Mol. Neurosci.* **8**, 78 (2016).

56. Kann, O. & Kovács, R. Mitochondria and neuronal activity. *Am. J. Physiol. Cell Physiol.* **292**, C641-657 (2007).

57. Harrold, C.L., *et al.* A functional overlap between actively transcribed genes and chromatin boundary elements. Preprint at *BioRxiv* https://doi.org/10.1101/2020.07.01.182089 (2020).

58. Zhao, Y.T., *et al.* Long genes linked to autism spectrum disorders harbor broad enhancer-like chromatin domains. *Genome Res.* **28**, 933-942 (2018).

59. Leidescher, S., *et al.* SPATIAL ORGANIZATION OF TRANSCRIBED EUKARYOTIC GENES. Preprint at *BioRxiv* https://doi.org/10.1101/2020.05.20.106591 (2020).

60. Gabel, H.W., *et al.* Disruption of DNA-methylation-dependent long gene repression in Rett syndrome. *Nature* **522**, 89-93 (2015).

61. McNaught, K.St.P., Belizaire, R., Isacson, O., Jenner, P., & Olanow, C.W. Altered proteasomal function in sporadic Parkinson's disease. *Exp. Neurol.* **179**, 38-46 (2003).

62. Hao, L., Yang, Z., & Lei, J. Underlying Mechanisms of Cooperativity, Input Specificity, and Associativity of Long-Term Potentiation Through a Positive Feedback of Local Protein Synthesis. *Front. Comput. Neurosci.* **12**, 25 (2018).

63. Monahan, K., *et al.* Cooperative interactions enable singular olfactory receptor expression in mouse olfactory neurons. *Elife* **6**, e28620 (2017).

64. Monahan, K., Horta, A. & Lomvardas, S. LHX2- and LDB1-mediated trans interactions regulate olfactory receptor choice. *Nature* **565**, 448-453 (2018).

65. Sawamoto, K., et al. Generation of dopaminergic neurons in the adult brain from mesencephalic precursor cells labeled with a nestin-GFP transgene. *J. Neurosci.* **21**, 3895-3903 (2001).

66. Matsushita, N., et al. Dynamics of tyrosine hydroxylase promoter activity during midbrain dopaminergic neuron development. *J. Neurochem.* **82**, 295-304 (2002).

67. Falcão, A.M., *et al.* Disease-specific oligodendrocyte lineage cells arise in multiple sclerosis. *Nat Med* **24**, 1837-1844 (2018).

68. Matsuoka, T., et al. Neural crest origins of the neck and shoulder. *Nature* **436**, 347-355 (2005).

69. Sousa, V.H., et al. Characterization of Nkx6-2-derived neocortical interneuron lineages. *Cereb. Cortex* **19** Suppl 1, i1-10 (2009).

70. Jaitner, C., et al. Satb2 determines miRNA expression and long-term memory in the adult central nervous system. *Elife* **5**, e17361 (2016).

71. Langmead, B. & Salzberg, S.L. Fast gapped-read alignment with Bowtie 2. *Nat. Methods* **9**, 357-359 (2012).

72. Quinlan, A.R. & Hall, I.M. BEDTools: a flexible suite of utilities for comparing genomic features. *Bioinformatics* **26**, 841-842 (2010).

73. Lex, A., *et al.* UpSet: Visualization of Intersecting Sets. *IEEE Trans. Vis. Comput. Graph.* **20**, 1983-1992 (2014).

74. Ying, Q.L., Stavridis, M., Griffiths, D., Li, M. & Smith, A. Conversion of embryonic stem cells into neuroectodermal precursors in adherent monoculture. *Nat Biotechnol.* **21**, 183-186 (2003).

75. Kolodziejczyk, A.A., *et al.* Single Cell RNA-Sequencing of Pluripotent States Unlocks Modular Transcriptional Variation. *Cell Stem Cell* **17**, 471-485 (2015).

76. Dobin, A., *et al.* STAR: ultrafast universal RNA-seq aligner. *Bioinformatics* **29**, 15-21 (2013).

77. Li, B. & Dewey, C.N. RSEM: accurate transcript quantification from RNA-Seq data with or without a reference genome. *BMC Bioinformatics* **12**, 323 (2011).

78. Aronesty, E. ea-utils: Command-line tools for processing biological sequencing data. *The open bioinformatics journal* http://code.google.com/p/ea-utils: **7**, 602 (2011).

79. Kar, G., *et al.* Flipping between Polycomb repressed and active transcriptional states introduces noise in gene expression. *Nat. Commun.* **8**, 36 (2017).

80. Macosko, E.Z., *et al.* Highly Parallel Genome-wide Expression Profiling of Individual Cells Using Nanoliter Droplets. *Cell* **161**, 1202-1214 (2015).

81. McInnes, L., Healy, J., Saul, N. & Großberger, L. UMAP: Uniform Manifold Approximation and Projection. *The Journal of Open Source Software* doi: 10.21105/joss.00861.

82. Li, H., *et al.* The Sequence Alignment/Map format and SAMtools. *Bioinformatics* **25**, 2078-2079 (2009).

83. Ramirez, F., *et al.* deepTools2: a next generation web server for deep-sequencing data analysis. *Nucleic Acids Res.* **44**, W160-165 (2016).

84. Love, M.I., Huber, W. & Anders, S. Moderated estimation of fold change and dispersion for RNA-seq data with DESeq2. *Genome Biol.* **15**, 550 (2014).

85. Zambon, A.C., *et al.* GO-Elite: a flexible solution for pathway and ontology over-representation. *Bioinformatics* **28**, 2209-2210 (2012).

86. Barbieri, M. *et al.* Complexity of chromatin folding is captured by the strings and binders switch model. *Proc. Natl. Acad. Sci.* **109**, 16173–16178 (2012).

87. Chiariello, A. M., Annunziatella, C., Bianco, S., Esposito, A. & Nicodemi, M. Polymer physics of chromosome large-scale 3D organisation. *Sci. Rep.* **6**, 29775 (2016).

88. Fiorillo, L. *et al.* Inference of chromosome 3D structures from GAM data by a physics computational approach. *Methods* S1046-2023(18)30485-7. (2019)

89. Plimpton, S. Fast parallel algorithms for short-range molecular dynamics. *J. Comput. Phys.* **117**, 1–19 (1995).

90. Kremer, K. & Grest, G. S. Dynamics of entangled linear polymer melts: A molecular-dynamics simulation. *J. Chem. Phys.* **92**, 5057–5086 (1990)

91. Annunziatella, C. *et al. Molecular Dynamics simulations of the Strings and Binders Switch model of chromatin*. *Methods* **142**, 81-88 (2018).

92. Kulakovskiy, I.V., *et al.* HOCOMOCO: towards a complete collection of transcription factor binding models for human and mouse via large-scale ChIP-Seq analysis. *Nucleic Acids Res.* **46**, D252-D259 (2018).

93. Traag, V.A., Waltmann, L., & van Eck, N.J. From Louvain to Leiden: guaranteeing well-connected communities. *Sci. Rep.* **9**, 5233 (2019).

94. Kelly, S.T. leiden: R implementation of the Leiden algorithm. R package version 0.3.3, https://github.com/TomKellyGenetics/leiden (2019).

1050 **Acknowledgments**

1051 The authors thank Sheila Q. Xie and Azhaar Ashraf for help processing midbrain
1052 samples, Thomas M. Sparks for developing the NPMI normalisation pipeline,
1053 Catherine Baugher for developing the TF motif analysis pipeline, and the Pombo lab
1054 members for helpful discussions. AP and AA acknowledge support from the
1055 Helmholtz Association (Germany). AP and MN acknowledge support from the
1056 National Institutes of Health Common Fund 4D Nucleome Program grant
1057 U54DK107977, and the Berlin Institute of Health (BIH). AP and LZR acknowledge
1058 support by the Deutsche Forschungsgemeinschaft (DFG; German Research
1059 Foundation) International Research Training Group (IRTG2403). AP acknowledges
1060 support from the Deutsche Forschungsgemeinschaft (DFG; German Research
1061 Foundation) under Germany's Excellence Strategy – EXC-2049 – 390688087. GCB
1062 acknowledges European Union Horizon 2020/European Research Council
1063 Consolidator Grant (EPIScOPE no. 681893), Swedish Research Council (no. 2015-
1064 03558; 2019-01360), Swedish Brain Foundation (no. FO2017-0075), Knut and Alice
1065 Wallenberg Foundation (grant 2019-0107), The Swedish Society for Medical
1066 Research (SSMF, grant JUB2019), Ming Wai Lau Centre for Reparative Medicine
1067 and Karolinska Institutet. GD and GA acknowledge support from the Austrian FWF
1068 through DK W1206 "Signal Processing in Neurons" and SFB F44 "Cell Signaling in
1069 Chronic CNS Disorders", P25014-B24. MAU acknowledges funding by the Medical
1070 Research Council (UK) (U120085816) and a Royal Society University Research
1071 Fellowship. MN thanks support from CINECA ISCRA Grant HP10CYFPS5 and
1072 HP10CRTY8P, by computer resources at INFN and Scope at the University of Naples
1073 (MN). LW acknowledges the support of Ohio University's GERB program. IH was
1074 supported by a Boehringer Ingelheim Fonds PhD fellowship, and ETT by an EMBO

short-term fellowship (ASTF 336-2015). II-A was supported by a Long-Term Fellowship from the Federation of European Biochemical Societies (FEBS).

Author Contributions

AP designed the concept for this work; WW, MM, AA, EJP and AP collected animal tissues; WW, AK, IH, MM, LS and RK produced GAM datasets; WW, AK, IH, MM and LS optimised the experimental protocol; WW, AK, II-A, CJT and EI developed computational pipelines for bioinformatics and QC analyses of GAM data; AK and IIA performed QC analyses of GAM data; WW and AK performed bioinformatics analyses of GAM data; DS and CJT developed the melting TAD analysis; DS performed the melting TAD analysis of GAM data; ETT performed mESC culture experiments; WWN and CJT developed the differential contact analysis; WWN performed differential contact analysis of GAM data; ETT and AAK produced single-cell RNAseq data; LZR and DS performed RNA-seq analysis; LZR performed differential gene expression analyses; SB optimized polymer modeling and performed PRISMR analysis; SB and AMC produced models for polymer modeling; AMC performed statistical analyses of polymer models; LF and FM performed in-silico GAM experiments; YZ performed TF motif finding enrichment, network, and community analyses; SAT supervised scRNA-seq experiments; MM, GA, GD, MU and GCB supervised animal tissue collection and provided animal samples; AP supervised GAM experiments and bioinformatics analyses; VF, AA, and AP supervised the scRNA-seq analysis; MN supervised the polymer modeling and in-silico GAM; LW supervised the TF motif and network analyses; WW, AK, IH, LZR, DS, MM, YZ, SB, AMC, MN, LW, GCB and AP contributed to the interpretation of the results; WW wrote the first draft of the manuscript; WW and IH designed the figures;

WW, AK, IH, LZR, DS, YZ, SB, AMC, LW, and AP wrote the manuscript. All authors provided critical feedback and helped revise the manuscript. The authors consider WW, AK and IH to have contributed equally to this work. The authors also consider LZR and DS to have contributed equally to this work.

Competing interests

In the past 3 years, S.A.T. has acted as a consultant for Genentech and Roche, and is a remunerated member of Scientific Advisory Boards of Biogen, GlaxoSmithKline and Foresite Labs.

A.P. and M.N. hold a patent on 'Genome Architecture Mapping': Pombo, A., Edwards, P. A. W., Nicodemi, M., Beagrie, R. A. & Scialdone, A. Patent PCT/EP2015/079413 (2015).

Materials & Correspondence

Correspondence and material requests should be addressed to ana.pombo@mdc-berlin.de

1119 **Table 1. Summary of GAM datasets used in this study.** VTA DNs were selected
1120 based on immunofluorescence detection of tyrosine hydroxylase (TH) from two
1121 animals, an 8-week old wild-type mouse and a 10-week old mouse carrying a TH-
1122 GFP reporter. PGNs were selected based on their position within the CA1 pyramidal
1123 cell layer and detection using pan-histone as a nuclear marker, from two 8-week old
1124 wildtype littermate mice. Cortical OLGs were selected based on detection of GFP
1125 expression from a 3-week old Sox10-cre-LoxP-GFP mouse. GAM data from mESC
1126 (clone 46C) was previously published[9], and available from the 4DNucleome portal
1127 after quality control (https://data.4dnucleome.org/; **Supplemental Table 6**).
1128

Dataset	GAM samples collected (3NPs per sample)	**GAM samples passing Quality Control**	**Number of cells per dataset**	Samples that did not pass quality control			Water controls	% loci pairs detected at least once (50-kb resolution)
				Orphan windows >70%	Uniquely mapped reads <50,000	Cross-contam-inated		
DNs R1	656	**585**	**1755**	58	11	4	13	99.7
DNs R2	316	**291**	**873**	19	6	3	6	99.5
PGNs R1	218	**209**	**209**	7	2	0	2	99.9
PGNs R2	288	**275**	**275**	7	1	0	6	99.7
OLGs	336	**290**	**290**	46	4	3	0	98.8
mESCs	-	**249**	**747**	-	-	-	-	99.9

Methods

Animal maintenance

Collection of GAM data from dopaminergic neurons was performed using one C57Bl/6NCrl (RRID: IMSR_CR:027; WT) mouse which were purchased from Charles River, and from one TH-GFP (B6.Cg-Tg(TH-GFP)21-31/C57B6) mouse, obtained as previously described[64,65]. All procedures involving WT and TH-GFP animals were approved by the Imperial College London's Animal Welfare and Ethical Review Body. Adult male mice of age 2–3 months were used. All mice had access to food and water *ad libitum* and were kept on a 12 h:12 h day/night cycle. C57Bl/6NCrl and TH-GFP mice received an intraperitoneal (IP) injection of saline 14 days or 24 h prior to the tissue collection, respectively, and they were part of a larger experiment for a different study.

Collection of GAM data from somatosensory oligodendrocyte cells was performed using Sox10::Cre-RCE::loxP-EGFP[66] animals which were obtained by crossing Sox10::Cre animals[67] on a C57BL/6j genetic background with RCE::loxP-EGFP animals[68] on a C57BL/6xCD1 mixed genetic background, both available at The Jackson Laboratories. The Cre allele was maintained in hemizygosity while the reporter allele was maintained in hemi- or homozygosity. Experimental procedures for Sox10::Cre-RCE::loxP-EGFP animals were performed following the European directive 2010/63/EU, local Swedish directive L150/SJVFS/2019:9, Saknr L150 and Karolinska Institutet complementary guidelines for procurement and use of laboratory animals, Dnr 1937/03-640. The procedures described were approved by the local committee for ethical experiments on laboratory animals in Sweden (Stockholms Norra Djurförsöksetiska nämnd), lic.nr. 130/15. One male mouse was sacrificed at P21. Mice were housed to a maximum number of 5 per cage in individually ventilated cages with the following light/dark cycle: dawn 6:00-7:00, daylight 7:00-18:00, dusk 18:00-19:00, night 19:00-6:00.

Collection of GAM data from hippocampal CA1 pyramidal glutamatergic neurons was performed using two 19 week-old male *Satb2*$^{flox/flox}$ mice. C57Bl/6NCrl (RRID: IMSR_CR:027; WT) mice were purchased from Charles River, Satb2$^{flox/flox}$ mice that carry the floxed exon 4 have been previously described[69]. The experimental procedures were done according to the Austrian Animal Experimentation Ethics Board (Bundesministerium für Wissenschaft und Verkehr, Kommission für Tierversuchsangelegenheiten). All mice had access to food and water ad libitum and were kept on a 12 h:12 h day/night cycle.

Tissue fixation and preparation

WT, TH-GFP, and *Satb2*$^{flox/flox}$ mice were anaesthetised under isoflurane (4 %), given a lethal IP injection of pentobarbital (0.08 µl; 100 mg/ml; Euthatal), and transcardially perfused with 50 ml of ice-cold phosphate buffered saline (PBS) followed by 50-100 ml of 4% depolymerised paraformaldehyde (PFA; Electron microscopy grade, methanol free) in 250 mM HEPES-NaOH (pH 7.4-7.6).

1173 Sox10::Cre-RCE::loxP-EGFP animals were sacrificed with a ketaminol/xylazine
1174 intraperitoneal injection followed by transcardial perfusion with 20 ml PBS and 20 ml
1175 4% PFA in 250 mM HEPES (pH 7.4-7.6). From C57Bl/6NCrl or TH-GFP mice, brains
1176 were removed and the tissue containing the VTA were dissected from each
1177 hemisphere at room temperature, and quickly transferred to fixative. For *Satb2*$^{flox/flox}$
1178 mice, the CA1 field hippocampus was dissected from each hemisphere at room
1179 temperature. For Sox10Cre/RCE mice, brain tissue containing the somatosensory
1180 cortex was dissected at room temperature. Following dissection, tissue blocks were
1181 placed in 4% paraformaldehyde (PFA) in 250 mM HEPES-NaOH (pH 7.4-7.6) for
1182 post-fixation at 4°C for 1 h. Brains were then placed in 8% PFA in 250mM HEPES
1183 and incubated at 4°C for 2-3 h. Tissue blocks were then placed in 1% PFA in 250 mM
1184 HEPES and kept at 4°C until tissue was prepared for cryopreservation (up to 5 days,
1185 with daily solution changes).
1186
1187 ***Cryoblock preparation and cryosectioning***
1188 Fixed tissue samples from different brain regions were further dissected to
1189 produce ~1.5x3 mm tissue samples suitable for Tokuyasu cryosectioning[3] (**Extended**
1190 **Data Fig. 1a**), at room temperature in 1% PFA in 250 mM HEPES. For the
1191 hippocampus, the dorsal CA1 region was further isolated. Approximately 1-3 mm x 1-
1192 3 mm blocks were dissected from all brain regions and were further incubated in 4%
1193 PFA in 250 mM HEPES at 4°C for 1 h. The fixed tissue was transferred to 2.1 M
1194 sucrose in PBS and embedded 16-24 h, at 4°C, positioned at the top of copper stub
1195 holders suitable for ultracryomicrotomy and frozen in liquid nitrogen. Cryopreserved
1196 tissue samples are kept indefinitely immersed under liquid nitrogen.
1197
1198 Frozen tissue blocks were cryosectioned with a Ultracryomicrotome (Leica
1199 Biosystems, EM UC7), with an approximate thickness of 220-230nm (ref. [3]).
1200 Cryosections were captured in drops of 2.1 M sucrose in PBS solution suspended in
1201 a copper wire loop and transferred to 10 mm glass coverslips for confocal imaging, or
1202 onto a 4.0 µm polyethylene naphthalate (PEN; Leica Microsystems, 11600289)
1203 membrane on metal framed slides for laser microdissection.
1204
1205 ***Immunofluorescence detection for confocal microscopy***
1206 For confocal imaging, cryosections were incubated in sheep anti-tyrosine
1207 hydroxylase (TH, 1:500; Pel Freez Arkansas LLC, Cat#P60101-0), mouse anti-pan-
1208 histone H11-4 (1:500; Merck, Cat#MAB3422) or chicken anti-GFP (1:500; Abcam
1209 Cat#ab13970) followed by donkey anti-sheep or goat anti-chicken IgG conjugated
1210 with AlexaFluor-488 (for TH and GFP; Invitrogen) or donkey anti-mouse IgG
1211 conjugated with AlexaFluor-555 or AlexaFluor-488 (for pan-histone; Invitrogen).
1212
1213 For PGNs, cryosections were washed (3x, 30 min total) in PBS, permeabilized
1214 (5 min) in 0.3% Triton X-100 in PBS (v/v) and incubated (2 h, room temperature) in
1215 blocking solution (1% BSA (w/v), 5% FBS (w/v) (GibcoTM Cat#10270), 0.05% Triton
1216 X-100 (v/v) in PBS). After incubation (overnight, 4°C) with primary antibody in

1217 blocking solution, the cryosections were washed (3-5x; 30 min) in 0.025% Triton X-
1218 100 in PBS (v/v) and immunolabeled (1 h, room temperature) with secondary
1219 antibodies in blocking solution, followed by 3 (15 min) washes in PBS. Cryosections
1220 were then counterstained (5 min) with 0.5 µg/ml 4',6'-diamino-2-phenylindole (DAPI;
1221 Sigma-Aldrich® Cat#D9542) in PBS, and then rinsed in PBS and water. Coverslips
1222 were mounted in Mowiol® 4-88 solution in 5% glycerol, 0.1M Tris-HCl (pH 8.5).
1223
1224 The number of SATB2 positive cells present in the hippocampal CA1 area of
1225 the *Satb2*$^{flox/flox}$ control mice was determined by counting nuclei positive for the
1226 SATB2 immunostaining (1:100; Abcam, Cat#ab10563678). To avoid counting the
1227 same nuclei, only every 30th ultrathin section cut through the tissue was collected,
1228 and the remaining sections discarded. Twenty-five nuclei were identified in the
1229 pyramidal neurons layer per image in the DAPI channel only and SATB2-positive
1230 cells counted. We confirmed that within the CA1 layer most cells (96%) are pyramidal
1231 glutamatergic neurons (data not shown).
1232
1233 For DNs and OLGs, cryosections were washed (3x, 30min total) in PBS,
1234 quenched (20 min) in PBS containing 20mM glycine**,** then permeabilized (15 min) in
1235 0.1% Triton X-100 in PBS (v/v). Cryosections were then incubated (1h, room
1236 temperature) in blocking solution (1% BSA (w/v), 0.2% fish-skin gelatin (w/v), 0.05%
1237 casein (w/v) and 0.05% Tween-20 (v/v) in PBS). After incubation (overnight, 4°C) with
1238 the antibody in blocking solution, the cryosections were washed (3-5x; 1 h) in
1239 blocking solution and immunolabeled (1 h, room temperature) with secondary
1240 antibodies in blocking solution, followed by 3 (15 min) washes in 0.5% Tween-20 in
1241 PBS (v/v). Cryosections were then counterstained with 0.5 µg/ml DAPI in PBS, then
1242 rinsed in PBS. Coverslips were mounted in Mowiol® 4-88.
1243
1244 Digital images were acquired with a Leica TCS SP8-STED confocal
1245 microscope (Leica Microsystems) using a 63x oil-immersion objective (NA = 1.4) or a
1246 20x oil-immersion objective, using pinhole equivalent to 1 Airy disk. Images were
1247 acquired using 405 nm excitation and 420-480 nm emission for DAPI; 488 nm
1248 excitation and 505-530 nm emission for TH or GFP; and 555 nm excitation and 560
1249 nm emission using a long-pass filter at 1024x1024 pixel resolution. Images were
1250 processed using Fiji (version 2.0.0-rc-69/1.52p), where adjustments included the
1251 optimization of the dynamic signal range with contrast stretching.
1252
1253 ***Immunofluorescence detection for laser microdissection***
1254 For laser microdissection, cryosections on PEN membranes were washed,
1255 permeabilized and blocked as for confocal microscopy, and incubated with primary
1256 and secondary antibodies as indicated above except for the use of higher
1257 concentrations of primary antibodies, as follows: anti-TH (1:50), anti-pan-histone
1258 (1:50) or anti-GFP (1:50). Secondary antibodies were used at the same
1259 concentration. Cell staining was visualized using a Leica laser microdissection
1260 microscope (Leica Microsystems, LMD7000) using a 63x dry objective. Following
1261 detection of cellular sections of the cell types of choice containing nuclear slices

1262 (nuclear profiles; NPs), individual NPs were laser microdissected from the PEN
1263 membrane, and collected into PCR adhesive caps (AdhesiveStrip 8C opaque; Carl
1264 Zeiss Microscopy #415190-9161-000). We used multiplexGAM[9] where three NPs are
1265 collected into each adhesive cap, and the presence of NPs in each lid was confirmed
1266 with a 5x objective using a 420-480 nm emission filter. Control lids not containing
1267 nuclear profiles (water controls) were included for each dataset collection to keep
1268 track of contamination and noise amplification of whole genome amplification and
1269 library reactions, and can be found in **Supplemental Table 2**.
1270
1271 ***Whole genome amplification of nuclear profiles***
1272 Whole genome amplification (WGA) was performed using an in-house
1273 protocol. Briefly, NPs were lysed directly in the PCR adhesive caps for 4 or 24h at
1274 60°C in 1.2x lysis buffer (30 mM Tris-HCl pH 8.0, 2 mM EDTA pH 8.0, 800 mM
1275 Guanidinium-HCl, 5 % (v/v) Tween 20, 0.5 % (v/v) Triton X-100), containing 2.116
1276 units/ml QIAGEN **protease (**Qiagen, Cat#19155). After protease inactivation at 75°C
1277 for 30 min, the extracted DNA was amplified using random hexamer primers with an
1278 adaptor sequence. The pre-amplification step was done using 2x DeepVent mix (2x
1279 Thermo polymerase buffer (10x), 400**µ**m dNTPs, 4 mM $MgSO_4$ in ultrapure water),
1280 0.5 **µ**M GAT-7N primers (5′- GTG AGT GAT GGT TGA GGT AGT GTG GAG NNN
1281 NNN N) and 2 units/**µ**l DeepVent® (exo-) DNA polymerase (New England Biolabs,
1282 M0259L) in the programmable thermal cycler for 11 cycles. Primers that anneal to the
1283 general adaptor sequence were then used in a second exponential amplification
1284 reaction to increase the amount of product. The exponential amplification was done
1285 using 2x DeepVent mix, 10 mM dNTPs, 100 **µ**M GAM-COM primers (5′-GTG AGT
1286 GAT GGT TGA GGT AGT GTG GAG) and 2 units/**µ**l DeepVent (exo-) DNA
1287 polymerase in the programmable thermal cycler for 26 cycles. For some NPs from
1288 DNs (see Supplemental Table 1), WGA was performed using a WGA4 kit (Sigma-
1289 Aldrich) using the manufacturer's instructions.
1290
1291 ***GAM library preparation and high-throughput sequencing***
1292 Following WGA, the samples were purified using SPRI beads (0.725 or 1.7
1293 ratio of beads per sample volume). The DNA concentration of each purified sample
1294 was measured using the Quant-iT® Pico Green dsDNA assay kit (Invitrogen #P7589)
1295 according to manufacturer's instructions. GAM libraries were prepared using the
1296 Illumina Nextera XT library preparation kit (Illumina #FC-131-1096) following the
1297 manufacturer's instructions with an 80% reduced volume of reagents. Following
1298 library preparation, the DNA was purified using SPRI beads (1.7 ratio of beads per
1299 sample volume) and the concentration for each sample was measured using the
1300 Quant-iT® PicoGreen dsDNA assay. An equal amount of DNA from each sample was
1301 pooled together (up to 196 samples), and the final pool was additionally purified three
1302 times using the SPRI beads (1.7 ratio of beads per sample volume). The final pool of
1303 libraries was analyzed using DNA High Sensitivity on-chip electrophoresis on an
1304 Agilent 2100 Bioanalyzer to confirm removal of primer dimers and estimate the
1305 average size and DNA fragment size distribution in the pool. NGS libraries were
1306 sequenced on Illumina NextSeq 500 machine, according to manufacturer's

1307 instructions, using single-end 75 bp reads. The number of sequenced reads for each
1308 sample can be found in **Supplemental Table 2**.
1309
1310 ***GAM data sequence alignment***
1311 Sequenced reads from each GAM library were mapped to the mouse genome
1312 assembly GRCm38 (Dec. 2011, mm10) with Bowtie2 using default settings[70]. All non-
1313 uniquely mapped reads, reads with mapping quality <20 and PCR duplicates were
1314 excluded from further analyses.
1315
1316 ***GAM data window calling and sample quality control***
1317 Positive genomic windows that are present within ultrathin nuclear slices were
1318 identified for each GAM library. Briefly, the genome was split into equal-sized
1319 windows (50 kb), and number of nucleotides sequenced in each bin was calculated
1320 for each GAM sample with bedtools[71]. Next, we determined the percentage of orphan
1321 windows (i.e. positive windows that were flanked by two adjacent negative windows)
1322 for every percentile of the nucleotide coverage distribution and identified the
1323 percentile with the lowest percent of orphan windows for each GAM sample in the
1324 dataset. The number of nucleotides that corresponds to the percentile with lowest
1325 percent of orphan windows in each sample was used as optimal coverage threshold
1326 for window identification in each sample. Windows were called positive if the number
1327 of nucleotides sequenced in each bin was greater than the determined optimal
1328 threshold.
1329
1330 Each dataset was assessed for quality control by determining the percentage
1331 of orphan windows in each sample, number of uniquely mapped reads to the mouse
1332 genome, and correlations from cross-well contamination for every sample
1333 (**Supplemental Table 2**). Most GAM libraries passed the quality control analyses
1334 (86-96% in each dataset; **Extended Data Fig. 1b-d**). To assess the quality of
1335 sampling in each GAM dataset, we measured the frequency with which all possible
1336 intra-chromosomal pairs of genomic windows are found in the same GAM sample,
1337 and found that 98.8 – 99.9% of all mappable pairs of windows were sampled at least
1338 once at resolution 50 kb at all genomic distances. Each sample was considered to be
1339 of good quality if they had <70% orphan windows, >50,000 uniquely mapped reads,
1340 and a cross-well contamination score determined per collection plate of <0.4
1341 (Jaccard index). The number of samples in each cell type passing quality control is
1342 summarized in **Table 1**.
1343
1344 ***Publicly available GAM datasets from mouse embryonic stem cells (mESC)***
1345 For mESCs, GAM datasets were downloaded from 4D Nucleome portal
1346 (https://data.4dnucleome.org/). We used 249 x 3NP GAM datasets from mESCs
1347 (clone 46C) which were grown at 37°C in a 5% CO_2 incubator in Glasgow Modified
1348 Eagle's Medium, supplemented with 10% fetal bovine serum, 2 ng/ml LIF and 1 mM
1349 2-mercaptoethanol, on 0.1% gelatin-coated dishes. Cells were passaged every other
1350 day. After the last passage 24 h before harvesting, mESCs were re-plated in serum-

free ESGRO Complete Clonal Grade medium (Merck, Cat# SF001- B). The list of 4DN sample IDs is provided in **Supplemental Table 6**.

Visualization of pairwise chromatin contact matrices

To visualize GAM data, contact matrices were calculated using pointwise mutual information (PMI) for all pairs of windows genome-wide. PMI describes the difference between the probability of a pair of genomic windows being found in the same NP given both their joint distribution and their individual distributions across all NPs. PMI was calculated by the following formula, where p(x) and p(y) are the individual distributions of genomic windows x and y, respectively; and p(x,y) are their joint distribution:

(1) $PMI = \log(p(x,y) / p(x)p(y))$

PMI can be bounded between -1 and 1, to produce a normalized PMI (NPMI) value given by the following formula:

(2) $NPMI = PMI / (-\log p(x,y))$

Insulation score and topological domain boundary calling

TAD calling was performed by calculating insulation scores in NPMI GAM contact matrices at 50 kb resolution, as previously described[3,9]. The insulation score was computed individually for each cell type and biological replicate, with insulation square sizes ranging from 100 to 1000 kb. TAD boundaries were called using a 500kb-insulation square size and based on local minima of the insulation score. Within each dataset, boundaries that were touching or overlapping by at least 1 nucleotide were merged. Boundaries were further refined to consider only the minimum insulation score within the boundary and 1 window on each side, to produce a 3 bin “minimum insulation score” boundary. In comparisons of boundaries between different datasets, boundaries were considered different when separated by at least one genomic bin, i.e. if they are separated by at least 50 kb. In **Fig. 2c,** we considered the boundary coordinate as the genomic window within a boundary with the lowest insulation value. TAD border coordinates for all cell types can be found in **Supplemental Table 7**. UpSet plots for TAD border overlaps, compartments, and TF motif analyses were generated either with custom Python or R scripts, or using the *UpSetR* tool[72].

mESC cell culture for scRNA-seq

Mouse embryonic stem cells from the 46C clone, derived from E14tg2a and expressing GFP under *Sox1* promoter[73], were a kind gift from D. Henrique (Instituto de Medicina Molecular, Faculdade Medicina Lisboa, Lisbon, Portugal). mESCs were cultured as previously described[19], i.e. cells were routinely grown at 37°C, 5% (v/v) CO_2, on gelatine-coated (0.1% v/v) Nunc T25 flasks in GMEM medium (Invitrogen, Cat# 21710025), supplemented with 10% (v/v) Foetal Calf Serum (FCS; BioScience LifeSciences, Cat# 7.01, batch number 110006), 2000 U/ml Leukaemia inhibitory

1396 factor (LIF, Millipore, Cat# ESG1107), 0.1 mM beta-mercaptoethanol (Invitrogen,
1397 Cat# 31350-010), 2 mM L-glutamine (Invitrogen, Cat# 25030-024), 1 mM sodium
1398 pyruvate (Invitrogen, Cat# 11360039), 1% penicillin-streptomycin (Invitrogen, Cat#
1399 15140122), 1% MEM Non- Essential Amino Acids (Invitrogen, Cat# 11140035).
1400 Medium was changed every day and cells were split every other day. mESC batches
1401 all tested negative for Mycoplasma infection, performed according to the
1402 manufacturer's instructions (AppliChem, Cat#A3744,0020). Before collecting material
1403 for scRNA-seq, cells were grown for 48h in serum-free ESGRO Complete Clonal
1404 Grade Medium (Merck, Cat# SF001- B) supplemented with 1000 U/ml LIF, on
1405 gelatine (Sigma, Cat# G1393-100ml)-coated (0.1% v/v) Nunc 10 cm dishes, with a
1406 medium change after 24h.
1407
1408 ***Single-cell mRNA library preparation***
1409 Two batches (denoted batch A and B, respectively) of single-cell mRNA-seq
1410 libraries were prepared according to Fluidigm manual "Using the C1 Single-Cell Auto
1411 Prep System to Generate mRNA from Single Cells and Libraries for Sequencing".
1412 Cell suspension was loaded on 10-17 microns C1 Single-Cell Auto Prep IFC
1413 (Fluidigm, Cat# 100-5760, kit Cat# 100-6201). After loading, the chip was observed
1414 under the microscope to score cells as singlets, doublets, multiplets, debris or other.
1415 The chip was then loaded again on Fluidigm C1 and cDNA was synthesised and pre-
1416 amplified in the chip using Clontech SMARTer kit (Takara Clontech, Cat# 634833). In
1417 batch B, we included Spike-In Mix 1 (1:1000; Life Technologies, Cat# 4456740), as
1418 from the Fluidigm manual. Illumina sequencing libraries were prepared with Nextera
1419 XT kit (Illumina, Cat# FC- 131-1096) and Nextera Index Kit (Illumina, Cat# FC-131-
1420 1002), as previously described[74]. Libraries from each microfluidic chip (96 cells) were
1421 pooled and sequenced on 4 lanes on Illumina HiSeq 2000, 2x100bp paired-end
1422 (batch A) or 1 lane on Illumina HiSeq 2000, 2x125bp paired-end (batch B) in the
1423 Wellcome Trust Sanger Institute Sequencing Facility (**Supplemental Table 8**).
1424
1425 ***ScRNA-seq data processing: mapping and expression estimates***
1426 To calculate expression estimates, mRNA-seq reads were mapped with STAR
1427 (Spliced Transcripts Alignment to a Reference, v2.4.2a)[75] and processed with RSEM,
1428 using the 'single-cell-prior' option (RNA-Seq by Expectation- Maximization,
1429 v1.2.25)[76]. The references provided to STAR and RSEM were the gtf annotation from
1430 UCSC Known Genes (mm10, version 6) and the associated isoform-gene
1431 relationship information from the Known Isoforms table (UCSC), adding information
1432 for ERCCs sequences in samples from batch B. Tables were downloaded from the
1433 UCSC Table browser (http://genome.ucsc.edu/cgi- bin/hgTables) and, for ERCCs,
1434 from ThermoFisher website (www.thermofisher.com/order/catalog/product/4456739).
1435 Gene-level expression estimates in "Expected Counts" from RSEM were used for the
1436 analysis.
1437
1438 ***ScRNA-seq data processing: quality control***
1439 Cells scored as doublets, multiplets, or debris during visual inspection of the
1440 C1 chip were excluded from the analysis. Datasets were also excluded if any of the

following conditions were met: <500,000 reads (calculated using sam-stats from ea-utils.1.1.2-537)[77]; <60% of reads mapped (calculated with sam-stats); <50% reads mapped to mRNA (picard-tools-2.5.0, broadinstitute.github.io/picard/); >15% of reads mapped to chrM (sam-stats); if present, >20% of reads mapped to ERCCs (sam-stats). Correlations between previously published mESCs (clone 46C) mRNA-seq bulk[19] and the single-cell RNAseq mESC transcriptomes were performed to assess quality of the single cell data. Correlations were performed as previously described[78]. Average single cell expression was highly correlated with bulk RNA-seq (**Extended Data Fig. 2b**).

ScRNA-seq integration and analysis

To integrate single cell transcriptomes from brain cell types of interest, we selected p21-22 OLGs[16], p22-32 CA1 PGNs[17], and p21-26 VTA DNs[18], based on the cell type and subtype definitions provided in their respective publications. The matrices of counts provided in each publication, along with the single-cell mESC transcriptomes produced which passed QC, were normalized applying the LogNormalize method and scaled using Seurat[79]. The scaled data was used for a PCA analysis, followed by processing through dimensionality reduction using Uniform Manifold Approximation and Projection (UMAP)[80]. Subsequent clustering was performed using the Seurat R package[79], with default parameters. Single mESC transcriptomes from batch A and B clustered together, and were pooled for further analyses. Genes that could not be mapped to the chosen reference GTF were removed (UCSC; accessed from iGenomes July 17, 2015; https://support.illumina.com/sequencing/sequencing_software/igenome.html.

To generate bigwig tracks for visualization, raw fastq files from each cell type were pooled into one fastq file. Reads were mapped to the mouse genome (mm10) using STAR with default parameters but --outFilterMultimapNmax 10. Bam files were sorted and indexed using Samtools[81] and normalized (RPKM) bigwigs were generated using Deeptools[82] bamCoverage. To account for differences in the number of technical replicates in OLG samples, cells were divided into groups by number of runs (1,2 and 6). The median of the reads for the group with the lowest sequencing depth was used as a threshold to normalize the other groups (i.e. the rest of the fastq files were randomly downsampled to that number of reads). The three groups of raw reads were pooled together and processed by applying the same method as for the other cell types. Pseudo-bulk expression was determined using the Regularized Log (R-log) value for each gene (**Extended Data Fig. 2e-f).** In each cell type, only the genes with R-log values ≥2.5 in all pseudo-bulk replicates were considered expressed.

Differential gene expression analysis

For differential expression analysis for all cell types, pseudo-bulk replicate samples were obtained by randomly partitioning the total number of single cells per dataset into three groups and pooling all UMIs per gene of cells belonging to the same replicate. To determine differentially expressed (DE) genes, all 6 possible

pairwise comparisons between samples were performed using DEseq2 with default parameters[83]. Genes classified as DE in at least one comparison were considered for further analysis (adjusted p-value < 0.05; Benjamini-Hochberg multiple testing correction method). A summary table for the DE expression analysis of all cell types can be found in **Supplemental Table 9**. For transcription factor motif analysis, only the DE genes obtained from the comparison between DNs and PGNs were considered for further analysis (**Extended Data Fig. 5c**).

For *Olfr* differential expression analyses, PGNs were classified as positive for *Olfr* expression if at least one gene was detected (≥1 UMI per cell; 164 cells). Two pseudo-replicates were generated for *Olfr*-positive and Olfr-negative cells by dividing the cells in each class in two random groups and pooling all UMIs per gene. DEseq2 was applied to obtain DE genes (adjusted p-value < 0.05; Benjamini-Hochberg method)[83]. To obtain robust results, this process was performed 21 times and only the genes classified as DE in at least 14/21 (67%) of iterations were considered as DE genes for this analysis. A summary table for the robust genes found in the DE expression analysis can be found in **Supplemental Table 10.** The same method was applied for *Vmn* genes (total *Vmn*-expressing cells, 203 cells), *Vmn*-expressing cells that do not express *Olfr* genes (*Vmn* only; 135 cells, 10 iterations only), and for random subsets of cells with the same number of *Olfr*-positive cells (164 cells, 10 iterations only). For *Vmn* only and random subsets, genes classified as DE in at least 7/10 (70%) of iterations were considered as DE genes. Only 12 DE genes were found when comparing total *Vmn*-expressing PGNs to *Vmn*- cells (*Kcnq1ot1*, *Meg3*, *Sngh11*, and *Srrm2* were upregulated; *Aldoa*, *Basp1, Calm2, Lars2, Pfn2, Rtn1, Scg2* and *Sub1* were downregulated; **Extended Data Fig. 9f**). For *Vmn* only cells, only 2 DE genes were found (*Vmn2r29* upregulated; *Lars2* downregulated), and no robust differential genes were detected for the randomly partitioned cells.

Gene Ontology

Gene ontology (GO) term enrichment analysis was performed using GOElite (version 1.2.4)[84]. In **Fig. 2d**, all genes expressed in at least one cell type, annotated to mm10, were used as the background dataset. In **Fig. 4d**, all genes expressed in PGNs or DNs were used as the background dataset, in **Figs. 5c**, **5d** all unique genes were used, and in **Fig. 5i** all expressed PGN genes were used. Default parameters were used for the GO enrichment: GO terms that were enriched above the background (significant permuted p-values <0.05, 2000 permutations) were pruned to select the terms with the largest Z-score (>1.96) relative to all corresponding child or parent paths in a network of related terms (genes changed >2). GO terms which had a permuted p-value ≥ 0.01, contained fewer than 6 genes per GO term or from the 'cellular_component' ontology were not reported in the main figures. A full list of unfiltered GO terms can be found in **Supplemental Table 11**.

Modeling and in-silico GAM

To reconstruct 3D conformations of the *Nrxn3* locus we employed the Strings & Binders Switch (SBS) polymer model of chromatin[85,86]. In the SBS, a chromatin

region is modelled as a self-avoiding chain of beads, including different binding sites for diffusing, cognate, molecular binders. Binding sites of the same type can be bridged by their cognate binders, thus driving the polymer folding. The optimal SBS polymers for the *Nrxn3* locus in mESCs and DNs were inferred using PRISMR, a machine-learning-based procedure which finds the minimal arrangement of the polymer binding sites best describing input pairwise contact data, such as Hi-C[31] or GAM[87]. Here, PRISMR was applied to the GAM experimental data by considering the NPMI normalization on a 4.8Mb region around the *Nrxn3* gene (Chr12: 87,600,000-92,400,000; mm10) at 50kb resolution in mESCs and DNs. The procedure returned optimal SBS polymer chains made of 1440 beads, including 7 different types of binding sites, in both cell types.

Next, to generate thermodynamic ensembles of 3D conformations of the locus, molecular dynamics simulations were run of the optimal polymers, using the freely available LAMMPS software[88]. In those simulations, the system evolves according to Langevin equation, with dynamics parameters derived from classical polymer physics studies[89]. Polymers are first initialized in self-avoiding conformations and then left to evolve in order to reach their equilibrium globular phase[85]. Beads and binders have the same diameter $\sigma = 1$, expressed in dimensionless units, and experience a hard-core repulsion by use of a truncated Lennard-Jones (LJ) potential. Analogously, attractive interactions are modelled with short-ranged LJ potentials[85]. A range of affinities between beads and cognate binders were sampled in the weak biochemical range, from $3.0K_BT$ to $8.0K_BT$ (where K_B is the Boltzmann constant and T the system temperature). In addition, binders interact unspecifically with the polymer with a lower affinity, sampled from $0K_BT$ to $2.7K_BT$. For sake of simplicity, the same affinity strengths were used for all different binding site types. Total binder concentration was taken above the polymer coil-globule transition threshold[85]. For each of the considered cases, ensembles of up to ~500 distinct equilibrium configurations were derived. Full details about the model and simulations are discussed in Barbieri *et al.*[85] and Chiariello *et al.*[90].

In-silico GAM NPMI matrices were obtained from the ensemble of 3D structures by applying the *in-silico* GAM algorithm[10], here generalized to simulate the GAM protocol with 3NPs per GAM sample and to perform NPMI normalization. Specifically, the same number of slices were used as in the GAM experiments, 249x3NPs for mESCs and 585x3NPs for DNs. Pearson correlation coefficients were used to compare the *in-silico* and experimental NPMI GAM matrices.

Example of single 3D conformations were rendered by a third-order spline of the polymer beads positions, with regions of interest highlighted in different colors. To quantify the size and variability of the 3D structures in mESCs and DNs, the average gyration radius (R_g) was measured from the selected domains encompassing and surrounding the *Nrxn3* gene, expressed in dimensionless units σ in **Fig. 3e**, **Extended Data Fig. 4d**.

1576 ***Melting TAD discovery***
1577 To assess gene insulation differences, insulation square values at ten length
1578 scales (100 – 1000 kb) were calculated for genes >400 kb in length (n = 479).
1579 Cumulative probability distributions of insulation square values were calculated for
1580 each dataset, and the brain cells were compared to mESC probability distributions for
1581 each gene by computing the maximum distance between the distributions and
1582 applying a Kolmogorov-Smirnov test with a custom script in R. P-values were
1583 corrected for multiple testing using the Bonferroni method, and -log10 transformed to
1584 obtain a 'TAD melting score'. TAD melting scores for each gene in each comparison
1585 can be found in **Supplemental Table 3**. For visualization, empirical cumulative
1586 probabilities and insulation score values were smoothed using a Guassian kernel
1587 density estimate (adjust = 0.3).
1588
1589 To compare TAD melting scores with transcription across the entire gene,
1590 length scaled RPM values were obtained for genes longer than 400 kb. Coordinates
1591 of genes were obtained from patch 6 (2017 release) of the Genome Reference
1592 Consortium m38 build for improved accuracy. RefSeq assembly accession
1593 GCF_000001635.26 was downloaded from NCBI on the 2019-11-19. The number of
1594 reads overlapping each gene in each cell type was computed using SAMtools[81] with
1595 the following parameters: *samtools view -b -h -c -F 4*. To obtain Reads Per Million
1596 (RPM) in each cell type, the number of overlapping reads was divided by a per
1597 million scaling factor (SF) which is specific for the sequencing depth of each cell type
1598 (SF = total number of counts / 10^6). Length-scaled RPM values were obtained per
1599 gene with the following formula:
1600
1601 (1) Length-scaled RPM = RPM / (length of gene in bp / 10^6)
1602
1603 ***Determining differential contacts between GAM datasets***
1604 To determine significant differences in pairwise contacts between a pair of
1605 GAM datasets, genomic windows with low detection, defined as less than 2% of the
1606 distribution of all detected genomic windows for each chromosome, were removed
1607 from both datasets to be compared. Next, NPMI contact frequencies at each genomic
1608 distance of each chromosome were normalized by computing a Z-score
1609 transformation, and a differential matrix (D) was derived by subtracting the two Z-
1610 score normalized matrices. A 10 Mb distance threshold was applied after computing
1611 the normalized matrices. The top significant differential contacts were determined for
1612 each dataset by fitting a normal distribution for each chromosome in matrix D and
1613 defining the upper and lower 5% of values from the fitted curve.
1614
1615 ***Transcription factor binding site analysis***
1616 To find transcription factor binding (TF) motifs present within specific contacts,
1617 significant differential contacts were determined for DNs and PGNs. For each set of
1618 differential contacts, we also constructed three sets of randomly generated contacts,
1619 containing the same number of contacts at each genomic distance for each
1620 chromosome. Next, accessible regions within the significant contacts were

determined using scATAC-seq[37] or sc low-input chromatin accessibility (liDNase-seq)[38] for PGNs and DNs, respectively. To account for methodological differences, including lower sequencing depth in DNs, we considered only the PGN scATAC-seq peaks that occurred in >25 cells (of 273 total cells). Motif finding within accessible regions in significant contacts was performed using the Regulatory Genomics Toolbox (https://www.regulatory-genomics.org/motif-analysis/introduction/) with TF motifs (from the HOCOMOCO database, v11)[91] obtained for TFs expressed in either DNs or PGNs (R-log ≥ 2.5) to determine the percentage of windows containing each TF motif. Next, TF motifs were filtered based on percentage of windows containing the motif (>5%) and differential expression in either PGNs or DNs (-log10(adj. p value) > 3) resulting in 48 TF motifs for feature pair analysis (32 TF motifs from PGNs and 16 from DNs; see **Extended Data Fig**. **5d-e**).

For feature pair analysis, we considered the co-occurrence of motif pairs <**i**,**j**> in contacting windows <**w**,**x**>, wherein motif **i** occurs in window **w** and motif **j** occurs in window **x**. The number of contacts containing each pair of selected TF motifs (1128 heterotypic motif pairs and 48 homotypic motif pairs; 1176 total) was calculated, together with the percentage of total significant differential contacts in PGNs and DNs. These metrics were used to calculate an 'Info Gain' score and an 'Enrichment' score for each TF motif pair. The Info Gain score is a measure of how well a given TF motif pair distinguishes two datasets, in this case PGNs and DNs. Info Gain measures the decrease in total entropy that results from classifying each contact based on the presence of a particular TF motif pair. The total entropy (E_T) is calculated as a function of the number of contacts in significant windows for PGNs (P_A) and DNs (D_A), and the total number of contacts in significant windows, $T = P_A + D_A$:

(1) $E_T = -((P_A/T) * \log(P_A/T)) - ((D_A/T) * \log(D_A/T))$

The entropy for a given TF motif pair (E_{TF}) was calculated as a function of the number of contacts containing the TF motif pair for PGNs (P_{TF}) and DNs (D_{TF}), respective to P_A and D_A, given as:

(2) $E_{TF} = -((P_{TF}/(D_{TF}+P_{TF})) * \log(P_{TF}/(D_{TF}+P_{TF}))) - ((D_{TF}/(D_{TF}+P_{TF})) * \log(D_{TF}/(D_{TF}+P_{TF})))$

The background entropy (E_B) for the contacts not containing the TF motif pair for PGNs ($P'_{TF} = P_A-P_{TF}$) and DNs ($D'_{TF} = D_A-D_{TF}$) is calculated similarly:

(3) $E_B = -((P'_{TF}/(D'_{TF}+P'_{TF})) * \log(P'_{TF}/(D'_{TF}+P'_{TF}))) – ((D'_{TF}/(D'_{TF}+P'_{TF})) * \log(D'_{TF}/(D'_{TF}+P'_{TF})))$

Info Gain was then determined by subtracting the weighted entropies of the TF motif pair and background from the total entropy:

(4) Info Gain = E_T - ((D_{TF}+P_{TF})/(D_A+P_A))*E_{TF} - ((D'_{TF}+P'_{TF})/(D_A+P_A))*E_B

Finally, an Enrichment score was determined by the percentage of contacts in either PGNs or DNs, given by the formula:

(5) Enrichment = (P_{TF}/P_A) / (D_{TF}/D_A)

Info gain and Enrichment scores for all TF feature pair interactions, as well as differential expression values (In DNs compared to PGNs) for each TF motif can be found in **Supplemental Table 4.** The top feature pairs were selected based on the top Info Gain scores (10 feature pairs), and highest (PGN enrichment; 5 feature pairs) or lowest (DN enrichment; 5 feature pairs) Enrichment scores. Contact overlaps for top feature pairs were visualized using UpSet plots.

Network and community detection analysis of transcription factor binding sites in significant differential contacts

To determine the interconnectivity between different TF motifs found in accessible regions of significant differential contacts, the number of contacts for each pair of TF motifs (1176 interactions) was determined. After filtering pairs of TF motifs with <15,000 contacts, a network was built for each cell type with TF motifs as nodes and number of contacts as edges. To detect community membership, the Leiden algorithm was applied using the *leiden* package in R[92,93], with a resolution of 1.05 for both PGNs and DNs (**Fig. 4g**, **Supplemental Table 5**).

Identification of compartments A and B

For compartment analysis, matrices of co-segregation frequency were determined by the ratio of independent occurrence of a single positive window in each sample over the pairwise co-occurrence of pairs of positive windows in a given pair of genomic windows[3]. GAM co-segregation matrices at 250 kb resolution were assigned to either A- or B-compartments, as previously described[3]. Briefly, each chromosome was represented as a matrix of observed interactions O(i,j) between locus i and locus j (co-segregation), and separately for E(i,j) where each pair of genomic windows are the mean number of contacts with the same distance between i and j. A matrix of observed over expected values O/E(i,j) was produced by dividing O by E. A correlation matrix C(i,j) is produced between column i and column j of the O/E matrix. Principal component analysis was performed for the first 3 components on matrix C, before extracting the component with the best correlation to GC content. Loci with PCA eigenvector values with the same sign that correlate best with GC content were called A compartments, while regions with the opposite sign were B compartments. For visualizations and Pearson correlations between datasets, eigenvector values on the same chromosome in compartment A were normalized from 0 to 1, while values on the same chromosome in compartment B were normalized from -1 to 0. Compartments were considered common if they had the same compartment definition within the same genomic bin. Compartment changes

between cell types were computed after considering compartments that were common between biological replicates, unless otherwise indicated.

To identify and visualize gene expression differences among genes in changing compartments, K-means clustering was performed on triplicate pseudo-replicates of each cell type using a custom Python script (**Supplemental Fig**. **S8a-b**). The number of clusters were determined using the elbow method, with k-means = 6 for genes in B compartment in mESCs and A in brain cells, and k-means = 5 for A compartment in mESCs and B in brain cells.

Data availability

Raw fastq sequencing files for all samples from DN, PGN and OLG GAM datasets, together with non-normalized co-segregation matrices, normalized pair-wised chromatin contacts maps and raw GAM segregation tables have been submitted to the GEO repository under accession number GSE94364. Raw fastq sequencing files for mESC GAM datasets are available from 4DN data portal (https://data.4dnucleome.org/). The 4DN sample IDs for all samples used in the study are available in **Supplemental Table 6**. Raw single cell mESC transcriptome data are available from ENA data portal (https://www.ebi.ac.uk/ena/browser/home) The ENA sample IDs for all samples used in the study are available in **Supplemental Table 11**.